PARTICLE TRANSPORT OF LHD

K. TANAKA,[a]* K. KAWAHATA,[a] T. TOKUZAWA,[a] T. AKIYAMA,[a] M. YOKOYAMA,[a]
M. SHOJI,[a] C. A. MICHAEL,[b] L. N. VYACHESLAVOV,[c] S. MURAKAMI,[d]
A. WAKASA,[d] A. MISHCHENKO,[e] K. MURAOKA,[f] S. OKAJIMA,[f]
H. TAKENAGA,[g] and LHD EXPERIMENT GROUP[a]

[a]*National Institute for Fusion Science, Toki 509-5292, Japan*
[b]*EURATOM/UAKEA Fusion Association, Culham Science Centre, Oxfordshire OX14 3DB, United Kingdom*
[c]*Budker Institute of Nuclear Physics, 630090, Novosibirsk, Russia*
[d]*Kyoto University, Department of Nuclear Engineering, Kyoto 606-8501, Japan*
[e]*Max Planck Institut für Plasmaphysik, EURATOM-Association, D-17491 Greifswald, Germany*
[f]*Chubu University, School of Engineering, Kasugai 487-8501, Japan*
[g]*Japan Atomic Energy Agency, 801-1 Mukoyama, Naka 311-0193, Japan*

Received September 11, 2009
Accepted for Publication December 15, 2009

Particle confinement processes are studied in detail on the Large Helical Device (LHD). Diffusion coefficients (D) and convection velocities (V) are estimated from density modulation experiments. The magnetic configuration and collisionality are widely scanned in order to investigate parameter dependences of D and V. To study the effect of the magnetic configuration, magnetic axis positions (R_{ax}) are scanned from 3.5 to 3.9 m. This scan changes the magnetic ripples quite significantly, enabling the effects of neoclassical properties on measured values to be widely elucidated. Dependences of electron temperature (T_e) and helically trapped normalized collisionality are examined using the heating power scan of neutral beam injection. It was found that generally larger (or smaller) contributions of neoclassical transport in the core region, where normalized position $\rho < 0.7$, resulted in more hollow (or peaked) density profiles. The larger neoclassical contribution was found to be situated at a more outwardly shifted R_{ax} for the same T_e and for higher T_e or lower ν_h^* at each R_{ax}. However, it is to be noted that $R_{ax} = 3.5$ m shows different characteristics from these trends, that is, a more peaked density profile at higher T_e or lower ν_h^*. The edge ($\rho > 0.7$) diffusion and convection are dominated by anomalous processes. Measured edge turbulence shows a possible linkage.

KEYWORDS: *particle transport, neoclassical transport, turbulence*

Note: Some figures in this paper are in color only in the electronic version.

I. INTRODUCTION

Control of density profiles is one of the important issues for future reactor operation in order to optimize fusion output power and stabilize magnetohydrodynamic instability and microinstabilities. Therefore, it is of utmost importance to understand the physics mechanisms governing particle transport. In this chapter, the results of the systematic study of particle transport are described. The discharges analyzed were in a relatively low density regime of neutral beam injection (NBI)–heated plasma in LHD experiments, where the line-averaged densities were around 1 to 2.5×10^{19} m^{-3}. The collisionality covered the $1/\nu$ and plateau regimes, where the effect of neoclassical transport became evident. Also, it is to be noted that the collisionality in this experiment was almost in a collisionality regime similar to that of the database of the international stellarator scaling 2004 (ISS04) (Ref. 1). This collisionality regime will cover the future operational regime of heliotron-type reactors. Therefore, the results of the present study bear important implications.

Density profiles of LHD and their parameter dependences used in later analyses are summarized in Sec. II.

*E-mail: ktanaka@nifs.ac.jp

The analysis technique for estimating particle transport coefficients is described in Sec. III. Parameter dependences of particle transport coefficients are explained in Sec. IV. The effects of turbulence are shown and discussed in Sec. V, followed by a summary and discussions together with a description of future directions in Sec. VI.

II. DENSITY PROFILES OF LHD

II.A. Observed Changes in Density Profiles

Figure 1 shows electron temperature (T_e) and electron density (n_e) profiles under different discharge conditions. The profiles are obtained from the data set of density modulation experiments, which is described in Secs. III and IV. Density profiles were measured using a multichannel far-infrared (FIR) interferometer,[2] and electron temperature profiles were measured using YAG Thomson scattering equipment.[3] Figure 2 shows the chord position of the interferometer. The chords covered the whole region of the plasma cross section, as shown in Fig. 2, and 10 or 11 channels are used for Abel inversion of the interferometer for density profile reconstruction. A slice-and-stack technique combined with a precalculated equilibrium database were done for profile reconstruction from the line-integrated density profiles. Figure 3 shows examples of the time history of the line-integrated density, stored energy, H_α intensity, and gas fueling rate of density modulation experiments,[4] which are described in detail in the following section. As shown in Fig. 3a, the noise of the measured line density is negligible. The error due to the mechanical vibration is $\sim 1 \times 10^{16}$ m^{-3} and has a negligible effect on reconstruction. The main error source for the Abel inversion is the uncertainty of the chord position, which is ~5 mm. This introduced ~6% error in the reconstructed profiles.[2] Both n_e and T_e profiles are shown in flux surface coordinates. The appropriate flux surface was selected from the database to match the n_e and T_e profiles of the outboard and inboard minor radii. The label ρ is defined as the square root of the ratio of toroidal flux inside a particular area to that bounded by the entire region inside the last closed flux surface (LCFS), and the values of ρ are approximately equal to radial positions normalized by the averaged minor radius of the LCFS.

Figure 1 shows profiles of electron temperature (T_e) and density (n_e) at different discharge conditions. As seen in these figures, the density profiles change from peaked to hollow depending on discharge conditions, which is in clear contrast to tokamak discharges in that density profiles are peaked in most cases.[5–7] Here, we discuss the causes affecting density profiles at these discharge conditions, which include fueling, NBI power, magnetic configuration, strength of magnetic field, and direction of NBI.

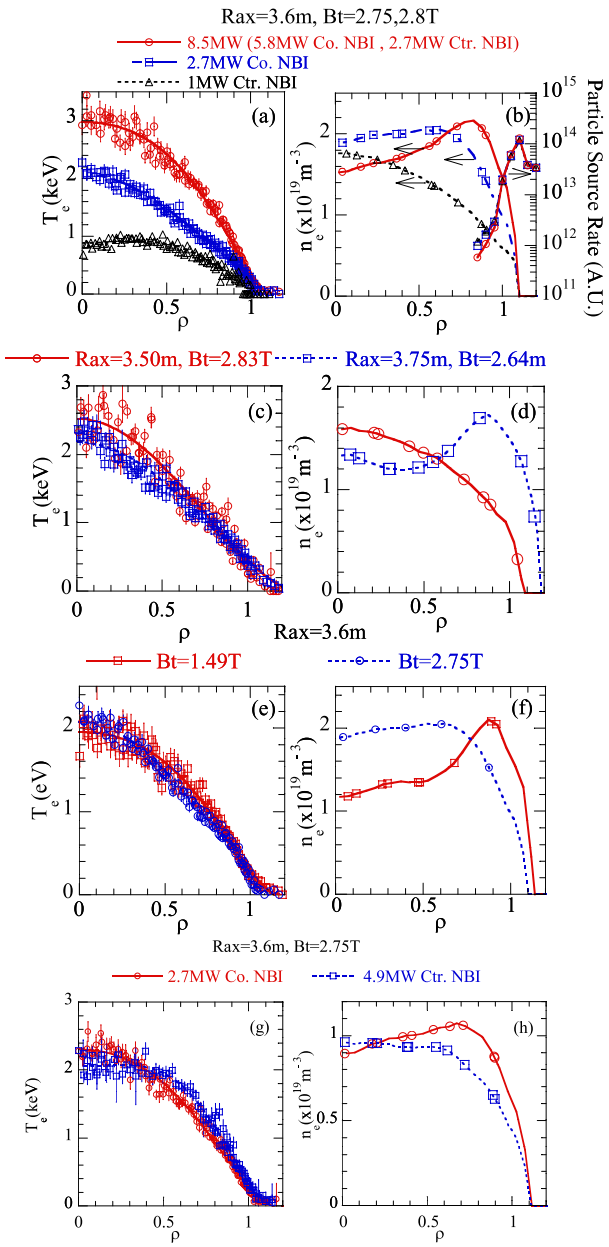

Fig. 1. Comparison of T_e (left side) and n_e (right side) profiles under different conditions. (a) and (b) Different NBI powers at $R_{ax} = 3.6$ m. (c) and (d) Different magnetic configurations at $R_{ax} = 3.5$ and 3.75 m. (e) and (f) Different magnetic fields at $R_{ax} = 3.6$ m. (g) and (h) Different directions of NBI at $R_{ax} = 3.6$ m. ρ is normalized position, and $\rho = 1$ corresponds to the last closed flux surface. Symbols of n_e profile chord position of FIR interferometer. The profiles of particle source rate are shown on the right side of (b).

Regarding fueling, we show that the different density profiles observed in Fig. 1 were not due to differences in particle fueling. Fueling sources were external gas fueling, wall recycling, and beam fueling. The

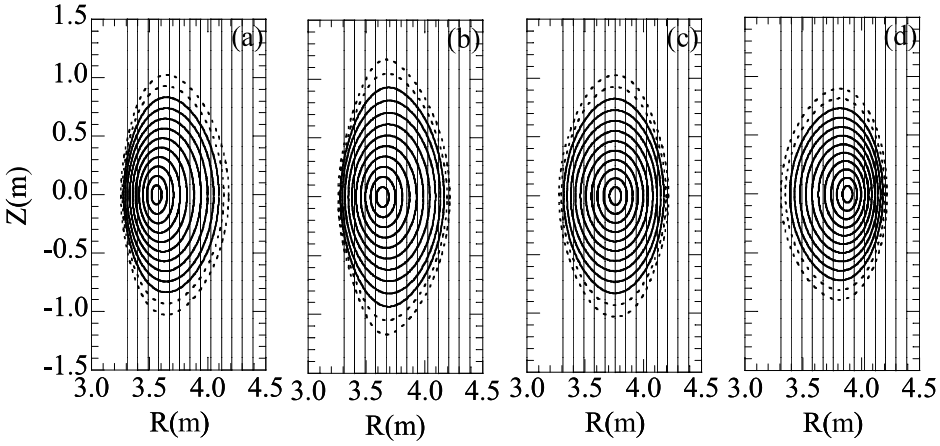

Fig. 2. Cross section of the 13-channel FIR laser interferometer. The $1/e^2$ intensity full width is 42 mm. Vacuum magnetic axis positions R_{ax} = (a) 3.5, (b) 3.6, (c) 3.75, and (d) 3.9 m. Vacuum flux surfaces are shown for the step of $\rho = 0.1$ with solid lines ($\rho = 0.1$ to -1.0) and with dashed lines ($\rho = 1.1$ and 1.2). ρ is normalized position.[2]

particle source rate spatial profiles from gas fueling and wall recycling were estimated using the three-dimensional (3-D) Monte Carlo simulation code DEGAS taking into account the 3-D structure of the vacuum vessel.[8] Presently, only relative profile shape of particle source rate is obtained. The results from the DEGAS code are shown in three profiles at the right side of Fig. 1b, which in fact overlapped each other in the figure. Three peaks existed at $\rho = 1.1$, and particle source rates decreased by one order of magnitude at $\rho = 1.0$. Thus, it is unlikely that these particle source rates could affect the density profiles. Also, beam fueling is not the dominant cause because, as shown in Figs. 1a and 1b, density profiles became more hollow with an increase of NBI power introducing larger beam fueling. If beam fueling determines the density profile, the density profile should be peaked with higher heating power. However, as shown in Fig. 1b, the observation is opposite. It should be noted that the NBI used in the series of experiments are all negative ion based and tangentially injected. The power of the negative ion–based NBI mainly comes from the acceleration voltage rather than from beam current. This is the other reason effects of the beam fueling are small.

Regarding NBI power, n_e profiles changed from peaked to hollow ones[4] with an increase of NBI power, as shown in Figs. 1a and 1b, whereas T_e increased with the shapes of T_e profiles (i.e., scale lengths of T_e) staying almost the same.[9] This fact suggests that the absolute values of T_e are important as a factor affecting density profiles, rather than its scale lengths.

Regarding magnetic configuration, the magnetic axis positions (R_{ax}) were changed. As shown in Figs. 1c and 1d, the density profile at $R_{ax} = 3.5$ m was peaked, whereas that at $R_{ax} = 3.75$ m (Refs. 5 and 10) was hollow with almost identical T_e profiles. The magnetic axis position greatly affects the properties of magnetic ripples, which in turn influence neoclassical transport. This fact may have caused the observed changes in density profiles, the details of which will be discussed later.

Regarding the strength of the magnetic field, the density profile at $B_t = 2.75$ T was flat, and that at $B_t = 1.49$ T was hollow, as shown in Fig. 1f, with almost the same T_e (Ref. 4).

Finally, regarding the direction of the NBI, the density profile for the coinjected NBI was hollow, and that for the counterinjection was flat, as shown in Fig. 1h. It is to be noted that the electron temperature profiles for the counterinjection were flattened from the peaked ones for the coinjection case for similar averaged temperatures, as shown in Fig. 1g.

The above-mentioned changes in density profiles are due to changes of externally controllable knobs. Later in this paper, we investigate the ruling physical mechanisms responsible for the observed density changes.

II.B. Dependences of Density Profiles on Collisionality and Magnetic Axis

Neoclassical transport is dictated by collisionality and magnetic ripple. The former is decided by electron temperature and density, which were scanned by NBI power, and the latter was changed by the position of the magnetic axes in the present set of experiments.

Dependence of neoclassical particle diffusion coefficients on normalized collisionality is shown in Fig. 4a for $R_{ax} = 3.5$, 3.6, 3.75, and 3.9 m. The calculation was carried out using the DCOM Monte Carlo simulation code[11] with monoenergetic particles. The diffusion coefficients in Fig. 4a are normalized by the plateau value of an equivalent circular tokamak, which has the same aspect ratio and rotational transform as that of

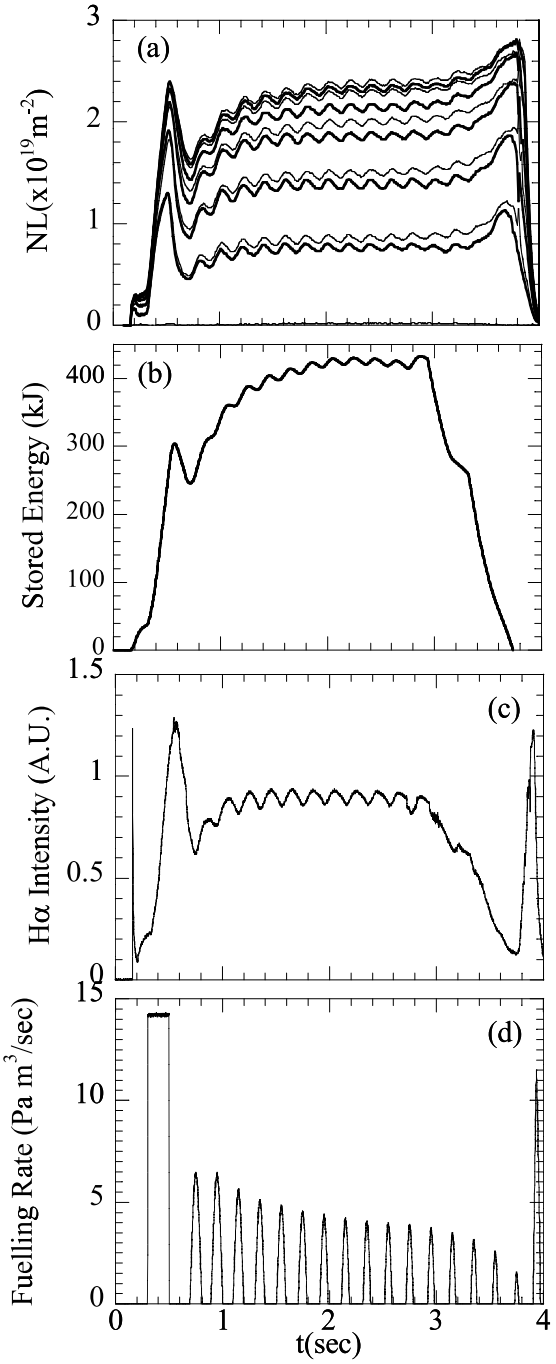

Fig. 3. (a) Example of 5-Hz modulated density at $R_{ax} = 3.6$ m. Thin lines indicate $R = 3.309$, 3.399, 3.489, 3.579, and 3.669 m (bottom to top). Thick lines indicate $R = 3.759$, 3.849, 3.939, 4.029, 4.119, and 4.209 (top to bottom). (b) H_α signal intensity and (c) gas puff fueling rate.[4]

LHD at each R_{ax}. The normalized diffusion coefficients are defined as $D_{\mathrm{LHD}}/D_{tokamak}$, where D_{LHD} is the diffusion coefficient of LHD and $D_{tokamak}$ is a plateau value of the equivalent circular tokamak $D_{tokamak} =$

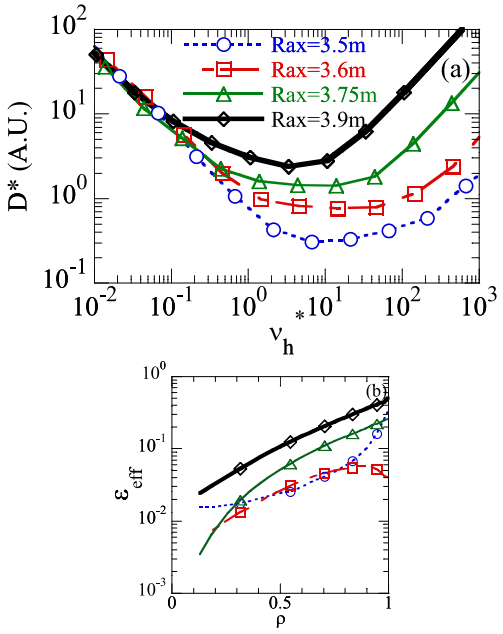

Fig. 4. (a) Collisionality dependence of normalized neoclassical diffusivity for monoenergetic particles calculated by DCOM. (b) Profiles of effective helical ripple.

$(\pi/16)(v^3/\iota R\omega_c^2)$, where v, R, ι, and ω_c are the electron velocity, the major radius, the rotational transform, and the cyclotron frequency, respectively. This normalization helps to illustrate the difference from the tokamak values. Since the calculation was done for monoenergetic particles, the integrations in velocity space are done to estimate values for particular plasma conditions with given n_e and T_e. The $1/\nu$ regime is evident at $\nu_h^* < 1$ for all R_{ax}. Here, the normalized collisionality ν_h^* is defined as follows:

$$\nu_h^* = \nu_{ei}/(\varepsilon_{eff}^{3/2} v_T/qR) \ , \tag{1}$$

where

ν_{ei} = electron-ion collision frequency

v_T = electron thermal velocity

q = safety factor

R = major radius

ε_{eff} = effective helical ripple.

This effective helical ripple is the representative value of the magnetic ripple amplitude for multiple helicity and is defined as[12]

$$\varepsilon_{eff} = \left(\frac{9\sqrt{2}}{16}\frac{\nu}{v_d^2}D\right)^{2/3} \ , \tag{2}$$

where

ν = collision frequency

v_d = drift velocity

D = particle diffusion coefficient

in the enhanced helical ripple–trapped region, which is the so-called $1/\nu$ region. In Eq. (1), the replacement of ε_{eff} by ε_t, which is the toroidal ripple, yields a well-known bounce frequency–normalized collisionality, which is widely used in tokamaks.

As shown in Fig. 4a, $\nu_h^* = 1$ is the approximate boundary between the $1/\nu$ and plateau regimes. Figure 4b shows profiles of ε_{eff} at four different magnetic axes. Effective helical ripples changed by around one order of magnitude for $R_{ax} = 3.5$ to 3.9 m. This causes significant changes in the neoclassical transport.

A more systematic comparison of density profiles under different conditions was carried out. The density peaking factor was defined as the ratio between density at $\rho = 0.2$ and the volume averaged density within the LCFS to describe density profiles quantitatively. Its dependence on ν_h^* is shown in Fig. 5. The data sets at high field ($B_t = 2.54$ to 2.8 T) and low field ($B_t = 1.45$ to 1.54 T) are shown in Figs. 5a and 5b, respectively. The scan of ν_h^* was realized by the change of R_{ax} and heating power under almost constant line-averaged density (1.0 to 2.5 $\times 10^{19}$ m^{-3}). The change of heating power scans ν_{ei} and that of R_{ax} scans ε_{eff}. As shown in Fig. 4b, the effective helical ripples became larger at the more outwardly shifted magnetic axes, resulting in a smaller ν_h^* for the same ν_{ei}. As shown in Fig. 5, the density peaking factors decreased with decreasing ν_h^*, indicating that n_e changes from a peaked to a hollow profile with decreasing ν_h^*. The clear dependence of density peaking factors on ν_h^* suggests a role of neoclassical transport on density profiles. This dependence is clearer at lower B_t, as shown in Fig. 5b. It should be noted that the magnetic axis moves outward due to the Shafranov shift from the R_{ax} in the vacuum. This becomes more evident at lower B_t.

The Shafranov shift could be one of the possible causes of the change in the density profile, because the plasma moves outward, where the helical ripple becomes larger.

Figure 6 shows the dependence of density peaking factors on the shifted magnetic axes. This figure includes both low- and high-field data. Here, the plasma axis shift was estimated from the Abel inversion of interferometer data.[2] Decreases of peaking factors with increases in shifted magnetic axes are clearly seen. For example, the density peaking factor at $R_{ax} = 3.53$ m for 1.45 T with a high heating power (low collisionality) is close to that at $R_{ax} = 3.75$ m for 2.64 T with a low heating power (high collisionality). This indicates that an outward shift of the magnetic axis due to the Shafranov shift is equivalent to an outward positioning of the magnetic axis by the external vertical field. In Fig. 6, it is shown that the density changed from peaked to hollow; i.e., the density peaking factor became less than unity when the shifted axis exceeded 3.7 m, whether the external or internal vertical field caused the axis shifts.

At higher B_t, this tendency cannot be seen at $R_{ax} =$ 3.5 m, as shown in Fig. 5a. The gradual increase of

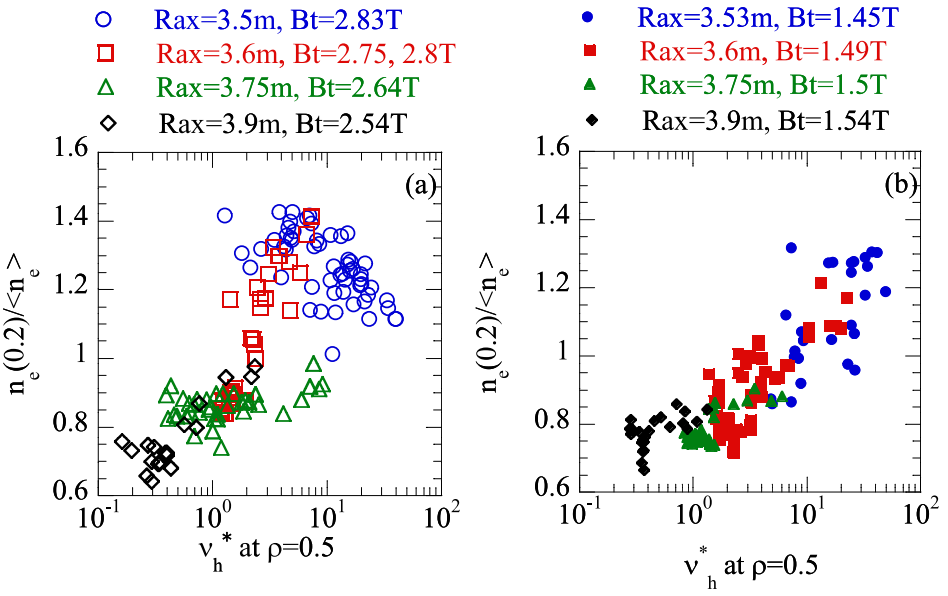

Fig. 5. Comparison of collisionality dependence of density peaking factor between four configuration of LHD at (a) high field ($B_t = 2.54$ to 2.8 T) (Ref. 5) and (b) low field ($B_t = 1.45$ to 1.54) (Ref. 10).

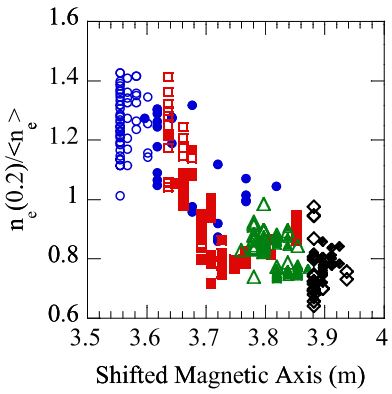

Fig. 6. Dependence of density peaking factor on shifted magnetic axis. The symbols are the same as those in Fig. 5 (Ref. 10).

peaking factors with decreasing ν_h^* is observed at $R_{ax} = 3.5$ m. This is characteristic for $R_{ax} = 3.5$ m at high field. The tendency at $R_{ax} = 3.5$ m is similar to the observation in tokamaks. In tokamaks, the density peaking factor increases with a decrease of the collisionality.[5–7] Theoretically, this can be understood to be due to the inward pinch driven by the ion temperature gradient (ITG) mode.[6,7] The observations at $R_{ax} = 3.5$ m may suggest the same mechanism.

III. ANALYSIS OF DENSITY MODULATION EXPERIMENT

In this section, the experimental technique and analysis techniques are briefly explained. The details are described in Refs. 4 and 13. The particle flux can be written as the sum of the diffusive term and the nondiffusive term:

$$\Gamma = -D\nabla n_e + n_e V \ . \tag{3}$$

The nondiffusive term is often called the convection term and can be driven by other gradients such as temperature, potential, momentum, etc. The particle balance equation is

$$\frac{\partial n_e}{\partial t} = -\nabla\cdot\Gamma + S = -\frac{1}{r}\frac{\partial}{\partial r} r\Gamma + S \ , \tag{4}$$

where S is particle source rate.

The difficulties in particle transport analysis are the existence of the convection term and the uncertainty of the particle source rate. It is impossible to obtain D and V separately from Eq. (4), because two unknown parameters cannot be obtained from one equation. The density modulation provides a modulation phase and amplitude. This effectively provides two sets of equations. For the modulated part of the density, the following equations are obtained in cylindrical geometry:

$$n_e = n_{e\,eq} + n_{emod} \ , \quad \Gamma = \Gamma_{eq} + \Gamma_{mod} \ , \quad S = S_{eq} + S_{mod} \ , \tag{5}$$

$$S_{mod} = \tilde{S}e^{i\omega t} \ , \quad n_{emod} = \tilde{n}_e e^{i\omega t} \ , \quad \partial n_{emod}/\partial t = i\omega\tilde{n}_e \ , \tag{6}$$

and

$$\frac{\partial^2\tilde{n}_e}{\partial r^2} + \left(\frac{1}{r} + \frac{1}{D}\frac{\partial D}{\partial r} - \frac{V}{D}\right)\frac{\partial\tilde{n}_e}{\partial r} - \left(\frac{V}{rD} + \frac{1}{D}\frac{\partial V}{\partial r}\right)\tilde{n}_e - i\frac{\omega}{D}\tilde{n}_e + \frac{\tilde{S}}{D} = 0 \ . \tag{7}$$

Here, the subscripts *eq* and *mod* indicate equilibrium and modulated quantities, and the tilde symbols and ω indicate modulation amplitude and frequency, respectively. As shown in Fig. 1b, the particle source rate is localized in the plasma edge; the modulated particle source induces a density perturbation propagating from the edge to the core. The parameters D and V characterize this propagation. From the analysis of the modulated components, D and V can be determined independently of the absolute value of the particle source rate, which is difficult to estimate experimentally. The particle source rate profiles are estimated by a neutral particle transport simulation code DEGAS (Ref. 8) and EIRENE (Ref. 14), which can take into account the three-dimensionally complicated shape of the LHD plasma and the vacuum vessel.

In Eq. (7), the neutral penetration speed is of the order of a kilometer per second, whereas the penetration speed of the density modulation is of the order of a meter per second. Therefore, the shape of the modulated particle source rate is assumed to be equal to that of the equilibrium one, and the spatial phase variation of the modulated source is neglected.

In Eq. (7), $\tilde{n}_e$ is a complex function ($\tilde{n}_e = \tilde{n}_{eR} + i\tilde{n}_{eI}$) consisting of real and imaginary parts as follows:

$$\frac{\partial^2\tilde{n}_{eR}}{\partial r^2} + \left(\frac{1}{r} + \frac{1}{D}\frac{\partial D}{\partial r} - \frac{V}{D}\right)\frac{\partial\tilde{n}_{eR}}{\partial r} - \left(\frac{V}{rD} + \frac{1}{D}\frac{\partial V}{\partial r}\right)\tilde{n}_{eR} + \frac{\omega}{D}\tilde{n}_{eI} + \frac{\tilde{S}}{D} = 0 \tag{8}$$

and

$$\frac{\partial^2\tilde{n}_{eI}}{\partial r^2} + \left(\frac{1}{r} + \frac{1}{D}\frac{\partial D}{\partial r} - \frac{V}{D}\right)\frac{\partial\tilde{n}_{eI}}{\partial r} - \left(\frac{V}{rD} + \frac{1}{D}\frac{\partial V}{\partial r}\right)\tilde{n}_{eI} - \frac{\omega}{D}\tilde{n}_{eR} = 0 \ . \tag{9}$$

Equations (8) and (9) are solved for the modeled D and V. The optimized D and V are determined to fit the calculated $\tilde{n}_{eR}, \tilde{n}_{eI}$ to measured ones to minimize the following χ^2 value:

$$\chi^2_{mod\_radial} = \int [(\tilde{n}_{eR\_exp} - \tilde{n}_{eR\_calc})^2 + (\tilde{n}_{eI\_exp} - \tilde{n}_{eI\_calc})^2]\, dr \ . \quad (10)$$

In Eq. (10), the subscripts *exp* and *calc* indicate experimentally observed values and values calculated from Eqs. (8) and (9) with assumed radial profiles of D and V and the radial profile of S from Monte Carlo simulation. The integration is along the minor radius. The spatial profiles of $\tilde{n}_{eR}$ and $\tilde{n}_{eI}$ are localized in the edge region. With the use of the presently available 10 or 11 channels of the FIR interferometer, reconstructions of $\tilde{n}_{eR}$ and $\tilde{n}_{eI}$ are difficult, especially with low diffusion or at high frequency modulation. In these cases, the reconstructed radial profile of the modulations suffers from contamination of reconstruction errors; therefore, we fit integrated values of $\tilde{n}_{eR\_calc}$ and $\tilde{n}_{eI\_calc}$ along the viewing chord of the interferometer, and the following χ^2 instead of Eq. (10) was used for fitting:

$$\chi^2_{mod\_int} = \sum_{ch} \left[\left(\int \tilde{n}_{eR\_exp}\, dl - \int \tilde{n}_{eR\_calc}\, dl \right)^2 + \left(\int \tilde{n}_{eI\_exp}\, dl - \int \tilde{n}_{eI\_calc}\, dl \right)^2 \right] . \quad (11)$$

In Eq. (11), the summation is a summation of each interferometer chord position's value and the integration is the integration along a viewing chord. In addition, the following χ^2 values are minimized simultaneously:

$$\chi^2_{eq} = \int (n_{eq\_exp} - \alpha \cdot n_{eq\_calc})^2\, dr \ . \quad (12)$$

In Eq. (12), n_{eq_exp} is the experimental equilibrium density profile, which is obtained from the density reconstruction, and n_{eq_calc} is the calculated density profile with the assumed D and V profiles and simulated S profile. As described above, the shape of the equilibrium source rate profile S_{eq} is assumed to be the modulated source rate profile $\tilde{S}$. The DEGAS and EIRENE simulation result does not give the absolute value of the equilibrium source rate profile. Therefore, the absolute value of n_{eq_calc}, which is calculated from Eq. (4) with the condition $dn_e/dt = 0$ for the equilibrium state, cannot be determined. Then, an additional fitting parameter α is used to match n_{eq_exp} and n_{eq_calc}.

Finally, a least-squares fitting is done to minimize the following χ^2:

$$\chi^2_{total} = \chi^2_{mod\_int} + weight \cdot \chi^2_{eq} \ . \quad (13)$$

The simultaneous minimization makes the fitting more stable. When the modulation amplitude is strongly localized in the edge region, the fitting of the $\chi^2_{mod\_int}$ becomes unstable. This is the case when the modulation frequency is high or D is small and V is largely outward. The parameter weight is tuned to minimize $\chi^2_{mod\_int}$ and χ^2_{eq} effectively. The parameter weight was tuned for the modulation frequency and set to be 1.0 for 2-Hz, 0.1 for 5-Hz, and 0.01 for 10-Hz modulation. The lower weight of the equilibrium fitting at higher modulation frequency is due to the smaller sensitivities of fitting of the modulation components at a higher modulation frequency.

The solutions of Eqs. (4) through (9) are in circular coordinates. To fit calculated values in circular coordinates to experimentally obtained values using Eq. (13), the radial position of the circular coordinate r in Eqs. (4) through (9) is converted to the normalized position ρ, which is $\rho = r/a_{\mathrm{LCFS}}$. Here, a_{LCFS} is the averaged minor radius of the LCFS. Precisely speaking, conversion from circular coordinates to a noncircular-shaped flux surface coordinate as in LHD requires a metric tensor; however, present analysis does not take this into account. The correction using the metric tensor can reduce the experimental D and V by a factor of 2 in the edge region. This does not affect the conclusion described in Sec. IV.

Figure 7 shows the models used for the fitting of D and V. When the modulation frequency is high or D is small or V is strongly outward, the modulation amplitude is localized in the edge, and the analysis becomes insensitive to core diffusion. Thus, the model of spatially constant D was used, as shown in Fig. 7a. When the modulation frequency is low or D is large or V is small or largely inward, the modulation penetrates deeply into the core. Thus, the two-parameter diffusion coefficient model was used, as shown in Fig. 7b, where the diffusion coefficient was assumed to change at $\rho = \rho_d$ with a transition width $\delta\rho$. The convection velocity was assumed to be zero at the plasma center and to increase linearly and change its slope at $\rho = \rho_v$.

In the model shown in Fig. 7, the value of ρ_d was fixed at 0.7 for all cases. For $R_{ax} = 3.5$ m at $B_t = 2.83$ T, $\delta\rho$ was fixed at 0.6 and ρ_v was fixed at 0.5. For other configurations ($R_{ax} = 3.6$, 3.75, and 3.9 m) when the modulation penetrated deeper to the core, $\delta\rho$ was fixed at

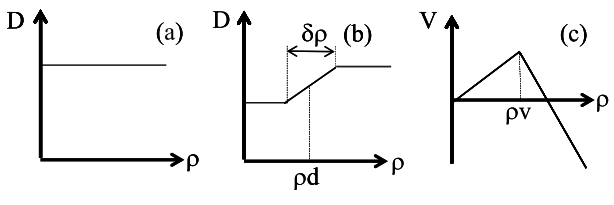

Fig. 7. Assumed profiles of D and V. (a) Spatially constant D for localized modulation amplitude, (b) two-variable D for core sensitive case, and (c) two-variable V for all cases.[10]

0.1 and ρ_d was fixed at 0.7. These values were determined a posteriori for good fitting.

The simultaneous fitting of modulation and equilibrium profiles requires additional consideration. The transport coefficients in the equilibrium state do not explicitly agree with transport coefficients from modulation experiments. This is due to the nonlinearity between the density gradient and the particle flux.[15] This effect was examined from a comparison of modulation-only fitting given by Eq. (11) and both equilibrium profiles and modulation fitting given by Eq. (13).

Figure 8 shows examples of the analysis at R_{ax} = 3.6 m, B_t = 2.8 T, P_{NBI} = 5.2 MW. The integrated amplitude and phase of the integrated amplitudes are shown. Two fitting schemes were compared: $\chi^2_{mod\_int}$ fitting using only modulation profiles given by Eq. (11) and χ^2_{total} fitting using both modulation and equilibrium profiles given by Eq. (13). Both schemes fit reasonably. The modeled D and V from the two fitting schemes are shown in Fig. 9. There are modest discrepancies between

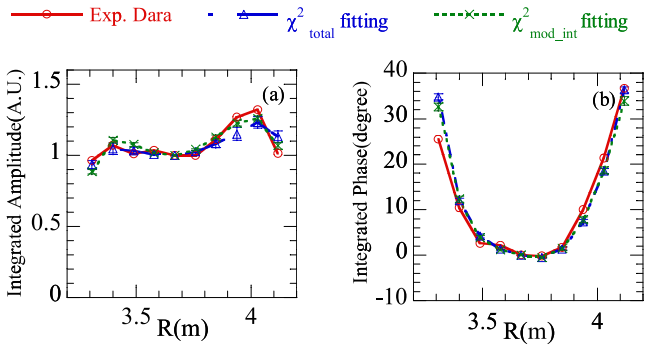

Fig. 8. Comparison of χ^2_{total} and $\chi^2_{mod\_int}$ fitting of integrated (a) amplitude, and (b) phase profiles; 5.2-MW NBI heating at R_{ax} = 3.6 m, B_t = 2.8 T.

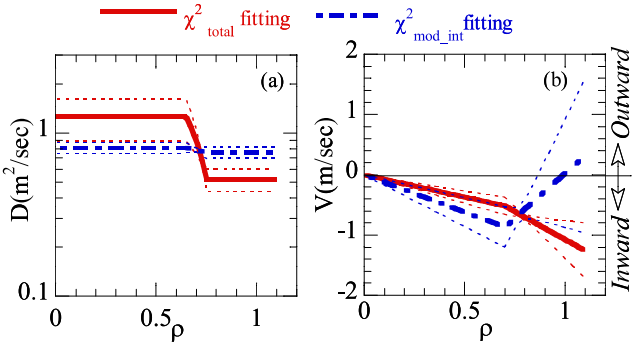

Fig. 9. Comparison of χ^2_{total} and $\chi^2_{mod\_int}$ fitting. (a) Diffusion coefficients profile and (b) convection velocity profile with 5.2-MW NBI heating at R_{ax} = 3.6 m, B_t = 2.8 T. The dotted thin lines indicate the upper and lower boundaries of the fitting errors.

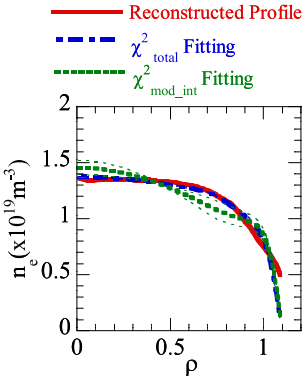

Fig. 10. Comparison of radial equilibrium profiles between profile reconstructed from Abel inversion and profiles calculated using χ^2_{total} and $\chi^2_{mod\_int}$ fitting. The dotted thin lines indicate the upper and lower boundaries of the fitting errors.

the two fitting schemes. Figure 10 shows a comparison of equilibrium profiles between measured and fitted profiles by using the D and V profiles of Fig. 9. In Fig. 9, the fitting error is negligible for χ^2_{total} fitting but not negligible for $\chi^2_{mod\_int}$ fitting. The larger fitting error for $\chi^2_{mod\_int}$ is due to a larger uncertainty in the convection velocity. Not significant but not negligible differences between two fitting schemes were observed, suggesting modest nonlinearity. Keeping this in mind, we did both equilibrium and modulation fitting schemes to get a stable solution.

IV. PARAMETER DEPENDENCES OF PARTICLE TRANSPORT

IV.A. Overview of Particle Transport at Different Magnetic Configurations

In this section, parameter dependences of particle transport coefficients (diffusion coefficient D and convection velocity V) at different magnetic axis positions are described. Changes in the magnetic positions of R_{ax} = 3.5 to 3.9 m permit ε_{eff} to be varied by around one order of magnitude, as seen from Fig. 4b, which in turn changes ν^*_h more than two orders of magnitude, as will be shown later. These changes significantly affect the transport property by neoclassical processes. Thus, experimentally estimated values of D and V are compared with neoclassical ones.

The present experiment was carried out at a high magnetic field of around B_t = 2.5 to 2.8 T. In a previous report,[16] most of the analyses were for a lower magnetic field of B_t = ~1.5 T. The lower magnetic field introduces a larger Shafranov shift due to the higher value of beta. As shown in Fig. 6, density peaking factors strongly

depend on the shifted magnetic axis position. Thus, once a plasma is shifted it functions as an outwardly shifted configuration. Therefore, a high magnetic field, yielding a small Shafranov shift, is suitable for investigating the effect of the magnetic axis position.

Figure 11 shows profiles of n_e, T_e, modulation amplitudes, D, and V at four different magnetic axis positions (R_{ax} = 3.5, 3.6, 3.75, and 3.9 m). The toroidal magnetic field was fixed at the maximum operational value for each magnetic axis position. The resulting small variation of B would not affect the transport property significantly. For example, transport coefficients for the maximum and minimum values of B in this experiment would be changed by 25% for B^{-2} scaling, as expected from gyro-Bohm or neoclassical processes.

As shown in Fig. 11, electron density profiles became more hollow at the more outward axis configurations, whereas electron temperature profiles stayed more or less the same.

In Fig. 11, two fitting variables for D (Fig. 7b) were used for R_{ax} = 3.5 and 3.9 m, and a spatially constant value of D (Fig. 7a) was used at R_{ax} = 3.6 and 3.75 m. As shown in Figs. 11c, 11h, 11m, and 11r, modulation amplitudes were found to be different. With higher

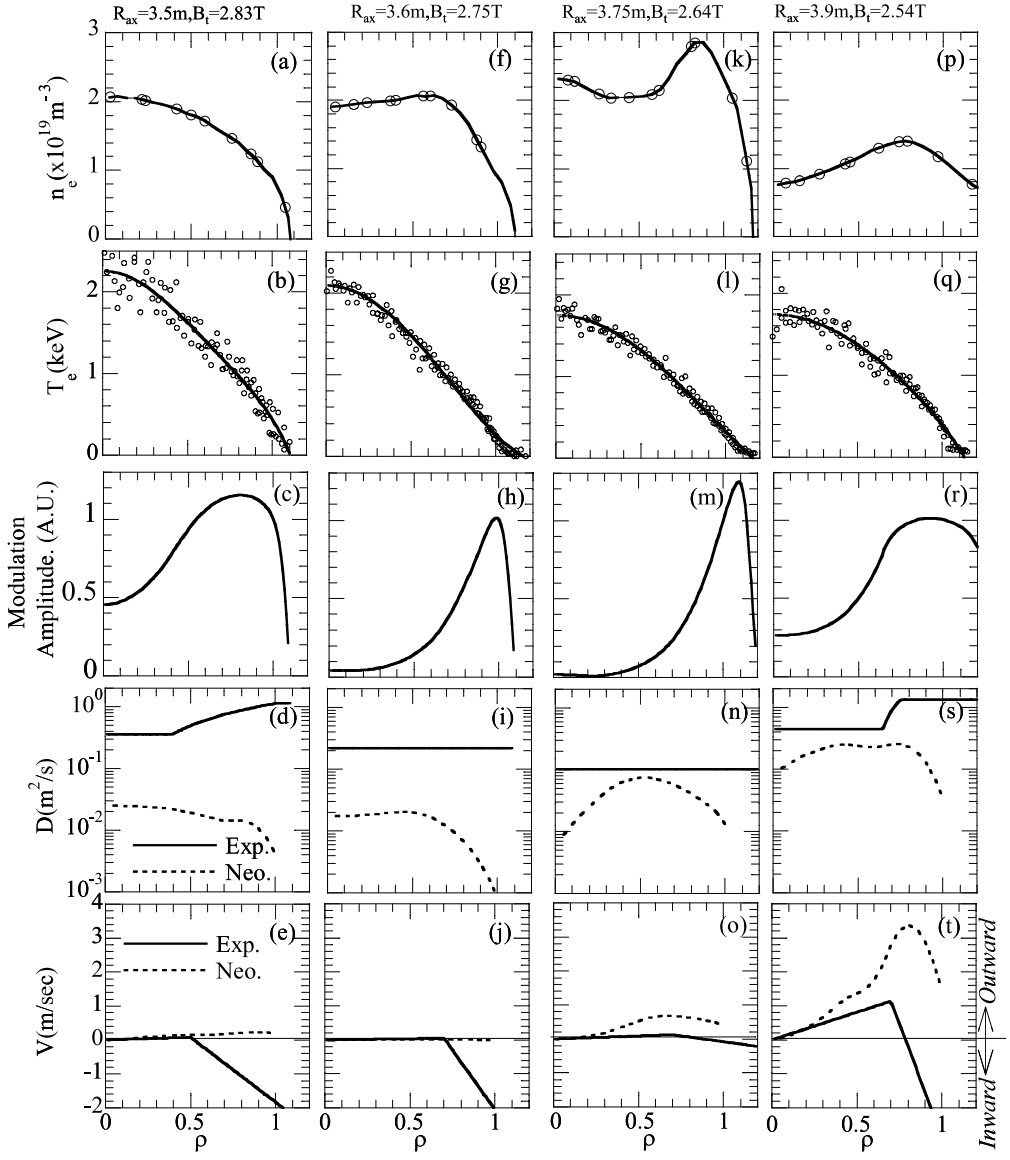

Fig. 11. Profiles of n_e, T_e, modulation amplitudes, D, and V. (a) through (e) R_{ax} = 3.5 m with B_t = 2.83 T. (f) through (j) R_{ax} = 3.6 m with B_t = 2.75 T. (k) through (o) R_{ax} = 3.75 m with B_t = 2.64 T. (p) through (t) R_{ax} = 3.9 m with B_t = 2.54 T. Modulation amplitudes are calculated values using estimated D and V. Modulation frequencies were 10 Hz at R_{ax} = 3.6 m and 5 Hz at other values of R_{ax}.

diffusion, modulation amplitudes penetrated deeply into the core region, as shown in Figs. 11c ($R_{ax} = 3.5$ m) and 11r ($R_{ax} = 3.9$ m), whereas with lower diffusion, they penetrated shallowly only at the edge, as shown in Figs. 11h ($R_{ax} = 3.6$ m) and 11m ($R_{ax} = 3.75$ m). The shallow penetration lacks sensitivity in the core region.

The neoclassical values of D and V were estimated using the DCOM code.[11] The neoclassical particle flux is given by[17]

$$\Gamma_{e\_neo} = -n_e D_1 \left[\frac{\nabla n_e}{n_e} + \frac{eE_r}{T_e} + \left(\frac{D_2}{D_1} - \frac{3}{2} \right) \frac{\nabla T_e}{T_e} \right] , \quad (14)$$

where D_1 is the neoclassical particle diffusion coefficient and E_r is the neoclassical E_r field, which is self-consistently determined to satisfy the ambipolarity condition by DCOM. The neoclassical particle convection velocity was defined from the comparison between Eqs. (3) and (14):

$$V_{e\_neo} = -D_1 \left[\frac{eE_r}{T_e} + \left(\frac{D_2}{D_1} - \frac{3}{2} \right) \frac{\nabla T_e}{T_e} \right] . \quad (15)$$

As shown in Figs. 11d and 11i, experimental values of D were more than one order of magnitude larger than those of the neoclassical predictions at $R_{ax} = 3.5$ and 3.6 m, respectively, over the whole spatial region, whereas experimental values of D became closer to neoclassical ones at around $\rho = 0.4$ to 0.7 for $R_{ax} = 3.75$ and 3.9 m, as shown in Figs. 11n and 11s, respectively. Figures 11e, 11j, 11o, and 11t indicate that neoclassical convection velocities are directed outwardly for all cases. In the data set of this section, the second term of Eq. (15), which is the so-called thermodiffusion term, dominated the first term, and the former was directed outwardly. This is in clear contrast to impurity transport, where the first term dominated the second term.[18] This is due to the high charge state of the impurities. At $R_{ax} = 3.6$, 3.75, and 3.9 m, experimental convection velocities at $\rho = 0$ to 0.7 became close to the neoclassical values of V, although experimentally determined values of V at $R_{ax} = 3.5$ m were directed inwardly and were opposite to the neoclassical prediction, which will be described in detail in Sec. IV.B.

IV.B. Dependences on Electron Temperature and Normalized Collisionality

In this section, the dependences of D and V on T_e and ν_h^* are studied at four different magnetic axis positions.

The temperature dependence forms the basis for the investigation of the neoclassical and anomalous transport model. For example, in the plateau and $1/\nu$ regimes of neoclassical transport, the diffusion coefficients are proportional to $T_e^{1.5}$ and $T_e^{3.5}$, respectively. Also, diffusion coefficients are proportional to $T_e^{1.5}$ in gyro-Bohm–like diffusion, where short-wavelength fluctuations (around the ion gyro-radius) play a role, and are proportional to T_e in Bohm-like diffusion, where particle transport is influenced by the long-wavelength fluctuations (up to the plasma minor radius). The convection velocities are the sum of off-diagonal transport coefficients; thus, it can have a T_e dependence.

The dependence on ν_h^* gives an idea of the contribution of neoclassical transport, as described in Sec. II.B.

Here, the core and edge values of D and V are studied. The core and edge values of D and V are taken from the averaged value at $\rho = 0.4$ to 0.7, defined as D_{core} and V_{core}, and at 0.7 to 1.0, defined as D_{edge} and V_{edge}, respectively. The comparisons with neoclassical values are also done. The neoclassical values are estimated from an integration of velocity space for the experimental plasma condition.

Figure 12 shows the electron temperature dependence of D and V estimated from experimental data (left column) and evaluated from the neoclassical prediction (right column). In later analyses, thus obtained values of D and V are fitted using an exponential function ($D = AT_e^B$) and a linear function ($V = C + DT_e$), respectively.

As shown in Figs. 12a, 12b, 12e, and 12f, both experimental and neoclassical D show positive T_e dependences. However, the experimental D is larger than the neoclassical D. Also, the temperature exponent index, which corresponds to the gradient of fitted line in Figs. 12a, 12b, 12e, and 12f, is clearly different for experimental and neoclassical D. The electron temperature exponent of D differs depending on R_{ax}. The exponent is the smallest at $R_{ax} = 3.6$ m for experimental and neoclassical D_{core} and D_{edge}.

As shown in Figs. 12a and 12b, D_{core} and D_{edge} of $R_{ax} = 3.75$ m are smaller than those of $R_{ax} = 3.6$ m at $T_e(\rho = 0.4 \text{ to } 0.7) < 1.4$ keV in the core region and in the whole experimental region of $T_e(\rho = 0.7 \text{ to } 1.0)$ in the edge region. However, since the T_e exponents of $R_{ax} = 3.75$ m are larger than those of $R_{ax} = 3.6$ m in both core and edge regions, D_{core} and D_{edge} of $R_{ax} = 3.75$ m become larger than those of $R_{ax} = 3.6$ m at higher T_e.

Except for the value of D_{edge} at $R_{ax} = 3.9$ m, indexes of electron temperature exponent for the neoclassical cases are larger than experimental ones.

Next, we focus our attention on V. The direction of V decides whether density profiles are hollow or peaked; namely, inwardly and outwardly directed convection velocities produce peaked and hollow density profiles, respectively.

Figures 12c and 12g show convection velocities at the plasma core ($\rho = 0.4$ to 0.7), determined experimentally ($V_{EXP.core}$) and neoclassically ($V_{NEO.core}$). $V_{NEO.core}$ shows the outward direction at all configurations, as shown in Fig. 12g. However, the direction of $V_{EXP.core}$ depended on R_{ax} and T_e, as shown in Fig. 12c. Values of $V_{EXP.core}$ at $R_{ax} = 3.5$ m were around zero at T_e ($\rho = 0.4$ to 0.7) < 1 keV and increased inwardly with increasing T_e at T_e ($\rho = 0.4$ to 0.7) > 1 keV, resulting in the

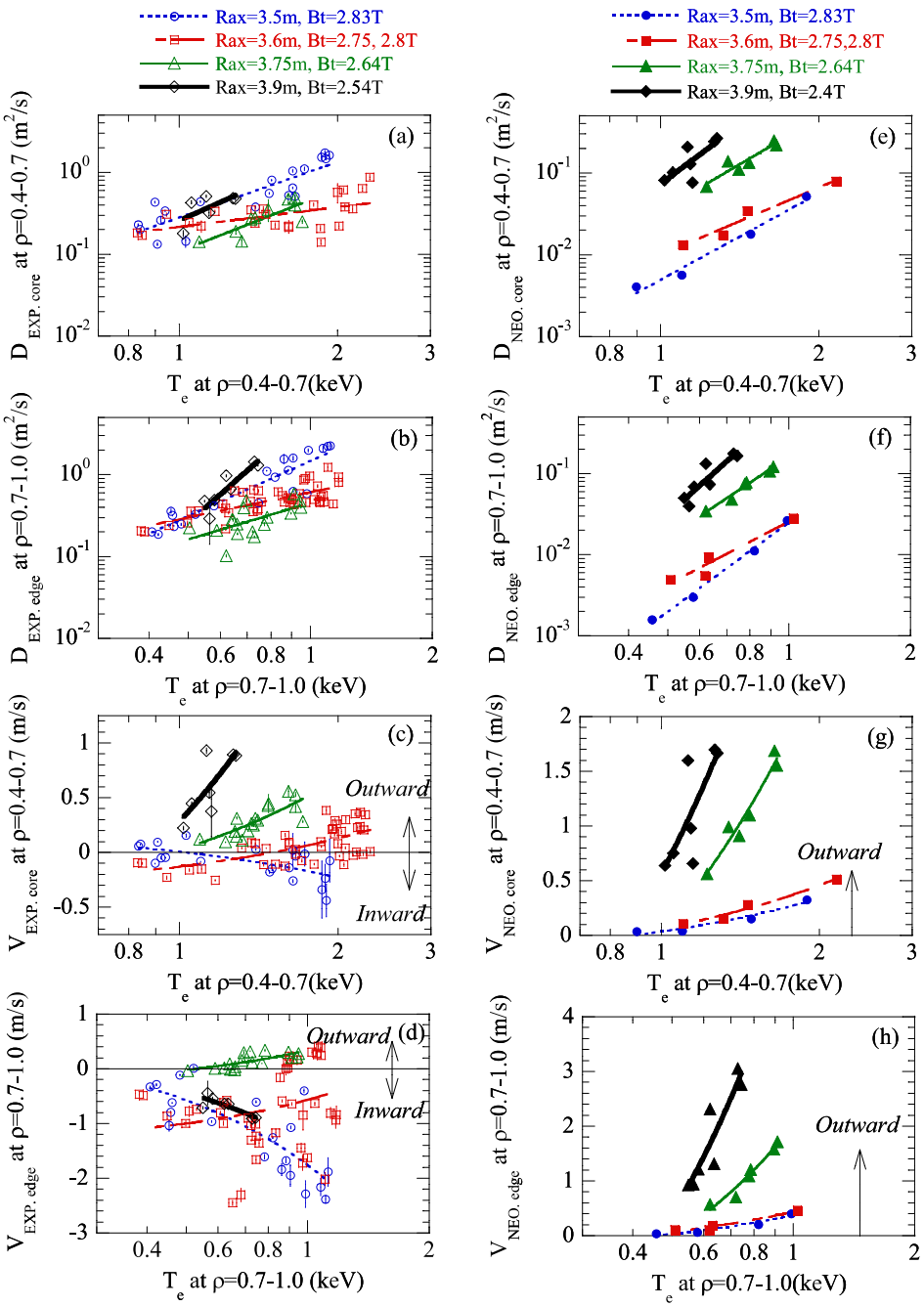

Fig. 12. Electron temperature dependences of (a) through (d) experimentally estimated and (e) through (h) neoclassically evaluated values of D and V. Error bars of experimental values came from fitting to experimental data. Electron temperatures were averaged over $\rho = 0.4$ to 0.7 for core values and over $\rho = 0.7$ to 1.0 for edge values. The dynamic range of the y-axis is the same for the right hand graph (experimental D and V) and the left hand graph (neoclassical D and V) although with different maxima and minima. Thus, the slope of the fitted lines can be compared between them.

gradual increase of the density peaking factor with decreasing ν_h^*, as shown in Fig. 5a. This is a different characteristic from other values of R_{ax} (R_{ax} = 3.6, 3.75, and 3.9 m), where values of $V_{EXP.core}$ increased outwardly with increasing T_e. At R_{ax} = 3.6 m, values of $V_{EXP.core}$ changed direction from inward to outward with increasing T_e, which is clearly reflected in Fig. 1b, where density profiles are peaked at low values of T_e and gradually hollow at higher T_e. At R_{ax} = 3.75 and 3.9 m, values of $V_{EXPcore}$ were always directed outwardly, resulting in density profiles that were hollow always.

Figures 12d and 12h show experimental and neoclassical V_{edge} ($\rho = 0.7$ to 1.0). Most experimental values of $V_{EXP.edge}$ were inwardly directed, although neoclassical values were always outwardly directed. The temperature dependence of $V_{EXP.edge}$ ($\rho = 0.7$ to 1.0) is not clear, suggesting the possibility of the existence of other hidden parameters to characterize $V_{EXP.edge}$.

Figure 13 shows the comparisons for different values of R_{ax}. Since both experimentally estimated and neoclassically evaluated values of D and V were a function of T_e, representative values are taken for the same values of T_e; namely, core and edge values are taken at T_e ($\rho =$ 0.4 to 0.7) = 1.25 keV and T_e ($\rho = 0.7$ to 1.0) = 0.65 keV using the fitting line in Fig. 12. These electron temperatures are selected from the achieved values over the whole R_{ax}. These are the highest achieved values at $R_{ax} = 3.9$ m. Figure 13 shows a comparison of the representative D and V. As shown in Figs. 13a and 13b, the neoclassical D_{core} and D_{edge} are a minimum at $R_{ax} = 3.5$ m; however, the experimental values are a minimum at $R_{ax} = 3.75$ m. This indicates that the experimental and neoclassical optimization are different for diffusion processes at the representative T_e. However, care must be taken. As shown in Figs. 12a and 12b, the minimum of the T_e exponent of the experimental D is at $R_{ax} = 3.6$ m. So, at higher T_e, the experimental minimum D may be at $R_{ax} = 3.6$ m.

The core diffusion coefficients at $R_{ax} = 3.5$ and 3.6 m are more than one order of magnitude larger than the neoclassical values, but those of $R_{ax} = 3.75$ and 3.9 m are around a factor of 2 larger. In the core region, the neoclassical contribution of D is negligible at $R_{ax} = 3.5$ and 3.6 m, but the neoclassical contribution becomes comparable to the experimental D at $R_{ax} = 3.75$ and 3.9 m. In the edge region, the experimental D exceeds the neoclassical by one or more orders of magnitude in all the configurations, indicating that edge diffusion is dominated by anomalous processes.

Figure 13c shows experimental and neoclassical V_{core} at $T_e = 1.25$ keV. Both experimental and neoclassical V_{core} have a minimum at $R_{ax} = 3.5$ m. However, V_{core} at $R_{ax} = 3.5$ and 3.6 m is inwardly directed at the representative T_e, although the neoclassical V_{core} is outwardly directed. In all configurations, the neoclassical V_{core} is larger than the experimental V_{core}. This indicates that the anomalous V_{core} is directed inward.

The absolute value of the experimental V_{core} is around half of the absolute value of the neoclassical V_{core}, although the direction of the experimental V_{core} is opposite to the neoclassical one at $R_{ax} = 3.5$ and 3.6 m.

Now, we turn our attention to the normalized collisionality (ν_h^*) dependences of D and V, which are shown in Fig. 14. As described in Sec. II, the normalized collisionality (ν_h^*) is an indication of the contribution of neoclassical transport and can be varied significantly for different R_{ax} due to the wide range of ε_{eff}. In the present data set of the experiment, the smaller ν_h^* indicates a larger contribution of neoclassical transport due to the $1/\nu$ effects.

As seen from Figs. 14a and 14b, experimentally estimated and neoclassically evaluated values of D_{core} and D_{edge} were larger at the lower values of ν_h^* for all configurations. Differences of both values of D_{core} and D_{edge} estimated experimentally from those evaluated neoclassically were smaller at the lower values of ν_h^*. These differences were smaller in the core region, suggesting that the neoclassical contribution to particle transport is more pronounced in the core region, while anomalous processes are dominating in the edge region.

Figures 14c and 14d show the dependences of experimentally estimated and neoclassically evaluated values of V_{core} and V_{edge} on values of ν_h^*. Neoclassically evaluated values of V_{core} had larger outward values than those estimated experimentally. Regarding magnetic axis dependence, experimentally estimated and neoclasically evaluated values of V_{core} for $R_{ax} = 3.6$, 3.75, and 3.9 m had about the same dependences on ν_h^* in that both increased outwardly with decreasing values of ν_h^*.

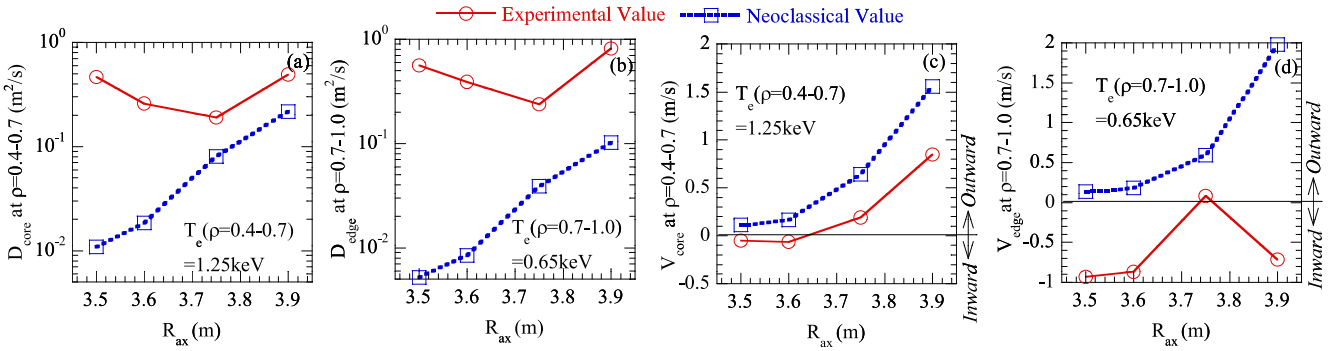

Fig. 13. Dependences of D and V on R_{ax} at the same values of T_e: (a) D_{core}, (b) D_{edge}, (c) V_{core}, and (d) V_{edge}. Core values were for $T_e = 1.25$ keV; edge values were for $T_e = 0.65$ keV. $B_t = 2.83$ T for $R_{ax} = 3.5$ m, 2.75 and 2.8 T for $R_{ax} = 3.6$ m, 2.64 T for $R_{ax} = 3.75$ m, and 2.54 T for $R_{ax} = 3.9$ m.

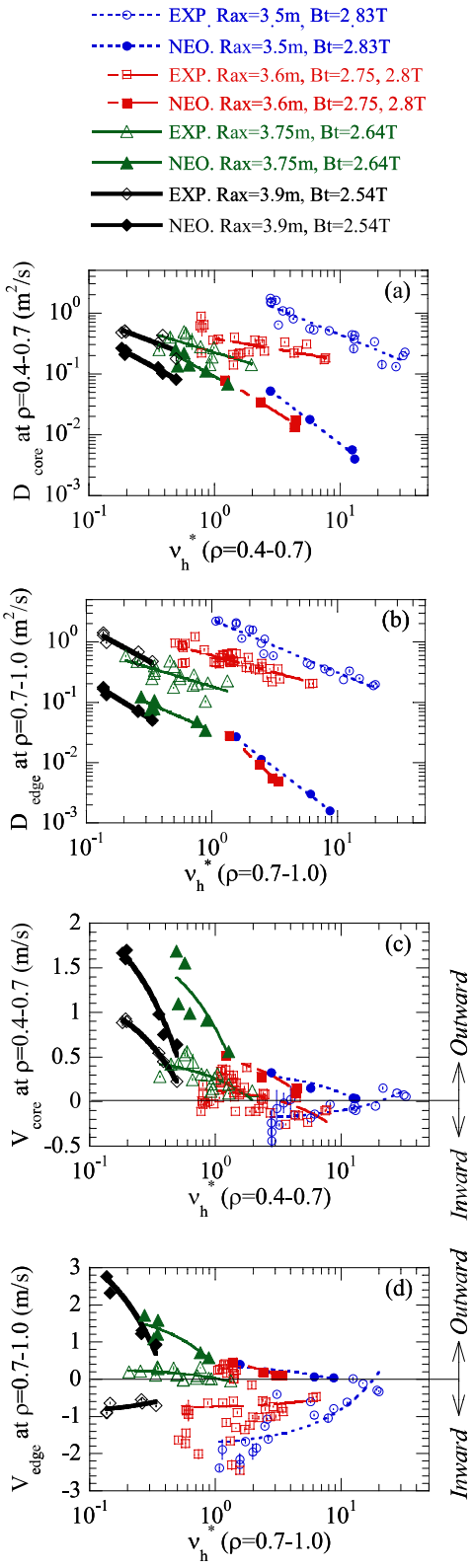

Fig. 14. ν_h^* dependence of experimentally estimated and neoclassically evaluated values of D and V: (a) D_{core}, (b) D_{edge}, (c) V_{core}, and (d) V_{edge}. ν_h^* is also averaged over $\rho = 0.4$ to 0.7 for core values and over $\rho = 0.7$ to 1.0 for edge values.

It should be noted that at $R_{ax} = 3.5$ m, the experimental V_{core} increase inwardly, whereas the neoclassical V_{core} increase outwardly with a decrease of ν_h^*. The core anomalous pinch, which is defined as the difference between the neoclassical and experimental V_{core}, at $R_{ax} = 3.5$ m shows an opposite ν_h^* dependence from the neoclassical pinch.

Neoclassical values of V_{edge} increased outwardly with decreasing values of ν_h^*. Experimental values of V_{edge} increased inwardly at $R_{ax} = 3.5$ and 3.6 m with decreasing values of ν_h^*, although data were scattered. Experimental values of V_{edge} at $R_{ax} = 3.75$ and 3.9 m did not show any trend at different values of ν_h^*.

IV.C. Toroidal Magnetic Field Dependence

To investigate the effects of magnetic fields on particle transport and their influence on density profiles, values of D_{edge} and V_{core} were evaluated for $R_{ax} = 3.6$ m at $B_t = 1.49$, 2.75, and 2.8 T. Most modulation experiments for $R_{ax} = 3.6$ m at $B_t = 1.49$ T were carried out at 10 Hz. Because it was found that outward convection was large and diffusion was modest, resulting in the measured phase shifts being relatively small, the model of a spatially constant value of D as shown in Fig. 7a was employed. We assume measured values to represent those at the edge, namely, D_{edge}.

Figure 15a shows a comparison of values of D_{edge} estimated experimentally and evaluated neoclassically. From this figure, one sees that all experimental data at different magnetic fields were about the same, whereas those from neoclassical evaluations differed by an order of magnitude at $B_t = 1.49$ and 2.75 T (2.8 T). It is to be noted that there are two possible effects due to different magnetic fields. The first is due to its absolute value and the other is due to the Shafranov shift. For the one order of magnitude difference in neoclassical evaluation shown in Fig. 15a, it was found that a factor of 3 is attributable to the Shafranov shift, being larger for smaller magnetic fields, and a factor of 3.5 due to the absolute magnitudes of the magnetic field.

Although Fig. 15a indicates that experimentally estimated absolute values of D_{edge} for different magnetic fields are more or less comparable, the temperature exponents were clearly different. The temperature exponents at 1.49 T and at 2.75 and 2.8 T were 2.5 and 1.0, respectively. The value at 1.49 T was clearly larger than that at 2.75 T (2.8 T). This is also interpreted as an effect of the Shafranov shifts, because the exponent became larger at the more outwardly shifted values of R_{ax}, as shown in Figs. 12a and 12b.

Most of the experimentally estimated values of V_{core} at $B_t = 1.49$ T were outwardly directed, as shown in Fig. 15b. This characteristic is also similar to that observed at $R_{ax} > 3.6$ m, suggesting that transport at a lower field with higher β becomes similar to that of an outward-shifted configuration.

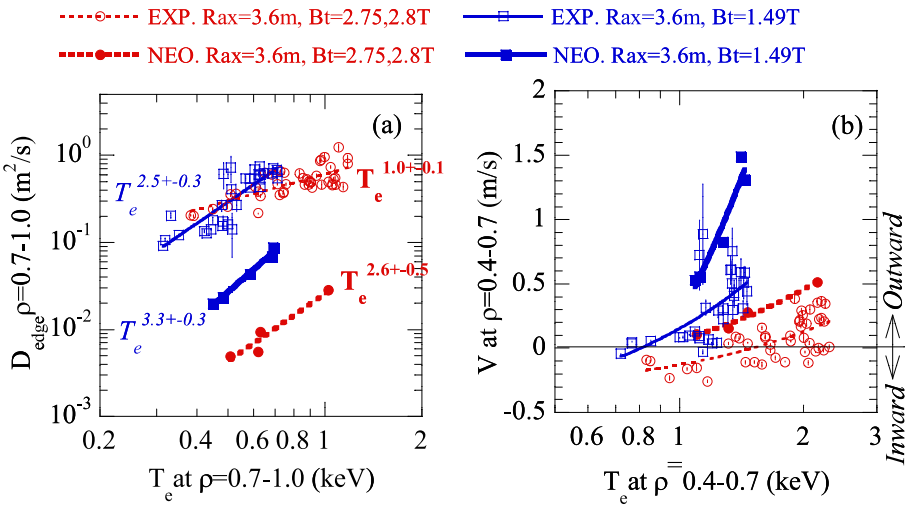

Fig. 15. Comparison of T_e dependence of (a) D_{edge} and (b) V_{core} for $R_{ax} = 3.6$ m at low field ($B_t = 1.49$ T) and high field ($B_t = 2.75$ and 2.8 T). In (a), italic and bold characters indicate T_e dependence at low and high field, respectively.

IV.D. Effect of Co- and Counter-NBI

As shown in Figs. 1g and 1h, with strong counter-NBI, both T_e and n_e profiles were flattened. The flattening is observed with strong counterinjection when the power is higher than about 4 MW. The counter-directed NBI-driven current produces a constant rotational transform (ι), which is 0.5 at $\rho < 0.5$ (Ref. 19). This can be interpreted as being due to the global stochastization.[19] Also, it can be interpreted as the formation of an $m/n = 2/1$ island from a heat pulse propagation study.[20] This observation is evident at $R_{ax} = 3.5$ and 3.6 m, where the magnetic hill parameter is larger than in other configurations. The core magnetic hill is likely an important parameter for the flattening of n_e and T_e with counter-directed NBI.

Figure 16 shows the comparison of the modulation amplitude, phase, and estimated D and V profiles between coinjection and counterinjection. Figure 16 was obtained from the same shot as Figs. 1g and 1h. As shown in Fig. 16a, with counter-NBI injection, the modulation penetrates to the core due to large core diffusion. The inward-directed pinch was observed in the whole region for counterinjection, whereas the outward-directed pinch was observed at $\rho = 0$ to 0.7 for the coinjected case. The large diffusion with strong counterinjection can be caused by the stochastization or island formation.

The flattening due to stochastization or island formation is clearly due to a different mechanism than the D and V dependences on T_e and ν_h^*. Therefore, we decided to exclude data from the strong counterinjection cases at $R_{ax} = 3.5$ and 3.6 m in the analysis described in Secs. IV.A, IV.B, and IV.C.

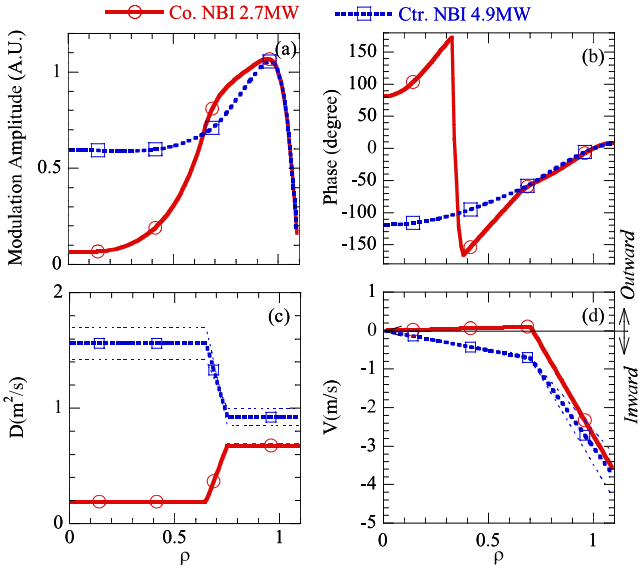

Fig. 16. Comparison of co- and counter-NBI injection: (a) modulation amplitude, (b) modulation phase, (c) D, and (d) V. These are estimated from the shot of Figs. 1g and 1h. The modulation amplitude and phases were calculated using estimated D and V.

IV.E. Correction of Previous Paper and Related Considerations

In a previously published paper by K. Tanaka et al., "Effect of Magnetic Configuration on Particle Transport and Density Fluctuation in LHD,"[16] there is a mistake on two graph labels. The vertical axis of Figs. 5c and 5d of

Ref. 16, which is $-\text{grad}\, T_e/T_e$ dependence of $V(\rho = 0.7)$ and $V(\rho = 1.0)$, should be corrected from $-\text{grad}\, T_e/T_e$ to $-\text{grad}\, T_e$. The normalized T_e gradient $-\text{grad}\, T_e/T_e$ is almost constant in the data set of Ref. 16 and the current paper. This is evident in Figs. 1a, 1c, and 1e and Figs. 11b, 11g, 11l, and 11q. This is likely due to the broad deposition of NBI. The constant $-\text{grad}\, T_e/T_e$ gives opportunities to consider the response of particle transport for different T_e under constant $-\text{grad}\, T_e/T_e$.

The core convection velocities are the most influential transport coefficients to determine density profiles. As shown in Fig. 12c, the $V_{EXP.core}$ shows a clear T_e dependence. As described in Sec. IV.B, the $V_{EXP.core}$ is dominated by the neoclassical convection velocities at $R_{ax} = 3.6$, 3.75, and 3.9 m, since its absolute value is comparable with the neoclassical value and the experimentally observed T_e and ν_h^* dependences are similar to those of neoclassical convection velocities. In the data set analyzed in the current paper, the neoclassical convection velocity described by Eq. (15) is dominated by the thermodiffusion term, which is the second term of Eq. (15). Therefore, the core convection velocities at $R_{ax} = 3.6$, 3.75, and 3.9 m are dominated by the neoclassical thermodiffusion. At $R_{ax} = 3.5$, the origin of the inward pinch is not understood yet. In tokamak theory, turbulence-driven thermodiffusion, turbulence-driven curvature pinch, and neoclassical Ware pinch are the candidates for the origin.[6,7] If tokamak turbulence theory can be applied at $R_{ax} = 3.5$ m, turbulence-driven thermodiffusion and curvature pinch are possible candidates. In Sec V.B and in Ref. 21, the curvature pinch was investigated in LHD, but it is not likely to account for the density profile of LHD. Therefore, at $R_{ax} = 3.5$ m, the turbulence-driven thermodiffusion is one of the possible origins to induce an inwardly directed pinch. This assumption, that convection is dominated by thermodiffusion, makes comparison between diffusion due to density gradient and temperature gradient possible in the same dimension. This comparison tells the character of particle transport.

The particle flux can be written as the sum of n_e gradient– and T_e gradient–driven fluxes:

$$\Gamma = -D\nabla n_e - D_t n_e \frac{\nabla T_e}{T_e} \quad , \tag{16}$$

where D is the particle diffusion coefficient of the diagonal term of the transport matrix and D_t is the thermodiffusion coefficient and one of the off-diagonal terms of the transport matrix. Then, the convection velocity was related to D_t from Eqs. (3) and (16) as follows:

$$D_t = -V \frac{T_e}{\nabla T_e} \quad . \tag{17}$$

The thermodiffusion coefficients are estimated over the whole R_{ax} using $V_{EXP.core}$ and the T_e profile. The discharges, where core temperatures at $\rho = 0.4$ to 0.7 are 1.1 ± 0.02 keV, are selected from the database of Fig. 12. Comparisons between D and D_t at each R_{ax} are shown in Fig. 17.

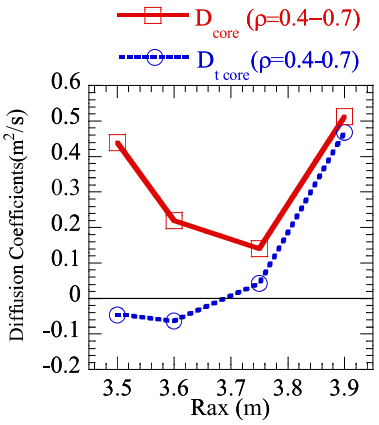

Fig. 17. Comparison of D_{core} ($\rho = 0.4$ to 0.7) and $D_{t\,core}$ ($\rho = 0.4$ to 0.7) at $T_{e\,core}$ ($\rho = 0.4$ to 0.7) $= 1.1 \pm 0.0225$ keV. Negative D_t at $R_{ax} = 3.5$ and 3.6 m indicates the existence of the inward pinch.

The thermodiffusion coefficients were negative at $R_{ax} = 3.5$ and 3.6 m due to the inwardly directed pinch at this T_e. The particle diffusion coefficients D are comparable with D_t at $R_{ax} = 3.75$ and 3.9 m. In the neoclassical values of the present data set, D_1 is around a factor of three larger than D_2 in Eq. (15). Thus, D_t is around a factor of 1.5 larger than D. But Fig. 17 shows that the experimental D exceeds D_t at $R_{ax} = 3.5$, 3.6, and 3.75 m and is comparable at $R_{ax} = 3.9$ m. The ratio becomes closer to the neoclassical one at more outward R_{ax}.

The normalized T_e gradient is almost constant in the data set. Thus, the increases of outwardly (inwardly) directed convection velocity with an increase of T_e at $R_{ax} =$ 3.6, 3.75, and 3.9 m ($R_{ax} = 3.5$ m) are not due to the increase of grad T_e/T_e in Eq. (16) but due to the positive (negative) T_e dependence of D_t.

V. EFFECT OF TURBULENCE

In this section, the role of turbulence in particle transport and turbulence modeling is discussed.

V.A. Experimental Observation of Turbulence Related to the Particle Transport

The contribution of neoclassical transport to the core diffusion becomes larger at lower ν_h^*, and its contribution to the core convection is comparable in the hollow profile of $R_{ax} = 3.6$ to 3.9 m; however, the neoclassical contribution to the edge diffusion is negligibly small for all configurations, as described in Sec. IV.B. Figure 18

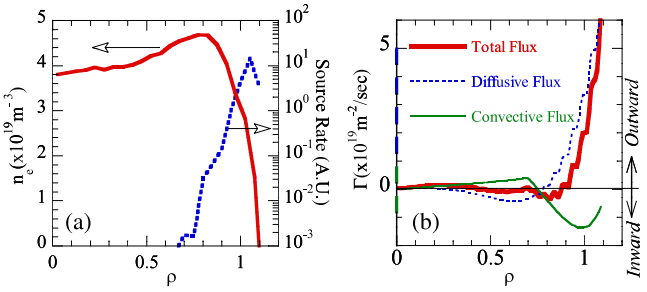

Fig. 18. (a) Density profile and particle source rate and (b) particle flux. $R_{ax} = 3.6$ m, $B_t = 2.75$ T (Ref. 16).

shows the density profile, particle source rate, and particle flux. The particle flux was estimated from Eq. (3) using the experimentally estimated D and V. As shown in Fig. 18b, in the edge region ($\rho > 0.9$), the particle flux is dominated by the diffusive flux. Thus, the turbulence amplitude was compared with the edge diffusion coefficients in the following investigations.

Microturbulence was measured by two-dimensional phase contrast imaging[22–24] (2-D PCI). Figure 19 shows the fluctuation profile measured by the 2-D PCI. The measurement ranges of 2-D PCI for Fig. 19 were $0.3 < k < 1.5$ mm^{-1} and $5 < f < 500$ kHz. The spatial resolution was around 10 to 30% of the average minor radius. Poloidally dominated wave number components are detected. The 2-D PCI can split the upper and lower part of the plasma cross section and can distinguish the propagation direction as the ion or electron diamagnetic direction in the laboratory frame.

Three different kinds of wave number components can be seen in Fig. 19b. In the outermost edge ($\rho > 1$), there are k values around 0.7 mm^{-1} propagating in the ion diamagnetic direction in the laboratory frame, and slightly farther in ($\rho \sim 0.9$), there are k values also around 0.7 mm^{-1} propagating in the electron diamagnetic direction in the laboratory frame. Toward the core ($\rho < 0.9$), there are low k values around 0.3 mm^{-1} propagating in the electron diamagnetic direction in the laboratory frame. The spatial resolution of the k components at $\rho < 0.9$ is poor. The upgraded system improved the spatial resolution of low k (Refs. 23 and 24). The normalized wave number $k\rho_s$, where ρ_s is the ion-sound Larmor radius, is around 0.5 for the whole region. This normalized wave number is in a linearly unstable region of the ion temperature gradient mode at $\rho = 0.6$ (Ref. 25).

Figure 19c shows the spatial profile of the phase velocity. The phase velocity was obtained from the ratio of frequency to wave number. The $E_r \times B_t$ rotation velocity is plotted in Fig. 19c as well. The radial electric field is calculated from the neoclassical ambipolar condition by using the GSRAKE code.[12] In Figure 19c, two branches are seen. One follows the $E_r \times B_t$ rotation velocity from the center toward the edge. This branch

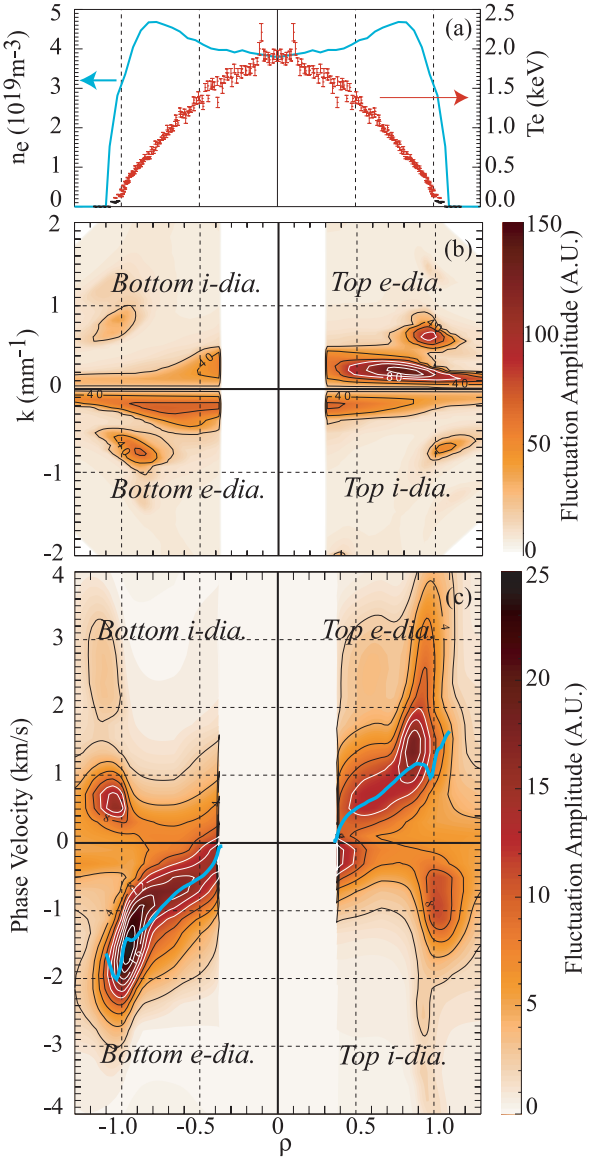

Fig. 19. (a) T_e and n_e profiles at $R_{ax} = 3.6$ m, $B_t = 2.75$ T, (b) spatial profile of wave number spectrum, and (c) spatial profile of velocity spectrum. Positive and negative ρ indicate above and below the equatorial plane, respectively. Positive k at positive ρ and negative k at negative ρ indicate the electron diamagnetic direction in the laboratory frame. Negative k at positive ρ and positive k at negative ρ indicate the ion diamagnetic direction in the laboratory frame. Thick solid lines indicate $E_r \times B_t$ rotation velocity.[16] E_r is calculated by GSRAKE from neoclassical ambipolarity condition.

consists of a low-k component in the core ($\rho < 0.9$) and a high k slightly inside the edge ($\rho \sim 0.9$), which are seen separately in Fig. 19b. This branch propagates in the electron diamagnetic direction in the laboratory frame and the phase velocity is around the $E_r \times B_t$

rotation velocity. The other branch has a high k in the outermost edge, which propagates in the ion diamagnetic direction in the laboratory frame. The existence of three different k branches is observed in the data set of the following investigation. The two components in the edge region, where one is an electron diamagnetic component at $\rho = 0.9$ and the other is an ion diamagnetic component at $\rho = 1.0$, are used to compare with D_{edge}.

The fluctuation response was measured at $R_{ax} = 3.6$, 3.75, and 3.9 m and compared with D_{edge}. The toroidal magnetic fields were 1.49, 1.5, and 1.54 T. Figure 20a shows the dependences of D_{edge} on R_{ax}. In Fig. 20, the edge diffusion coefficient of $R_{ax} = 3.6$ m is smaller than that of $R_{ax} = 3.75$ m, although the D_{edge} of $R_{ax} = 3.6$ m at $B_t = 2.75$ and 2.8 T was larger than that of $R_{ax} = 3.75$ at $B_t = 2.64$ T, as shown in Fig. 12b. As described in Sec. IV.C, the lower magnetic field introduces a larger magnetic axis shift due to the higher beta, so the effective R_{ax} for minimum D_{edge} at a lower field may be close to $R_{ax} = 3.75$ m and therefore is consistent with higher-field, low-beta results.

Figure 20b shows the relation between D_{edge} and the fluctuation level in the edge region of the electron and ion diamagnetic propagating components. Here, the fluctuation level is the ratio of the observed fluctuation amplitude, which is averaged between $\rho = 0.7$ and 1.1, $k > 0.5$ mm^{-1}, and $5 < f < 500$ kHz, to the averaged density at $0.7 < \rho < 1.1$. Because the spatial resolutions of the fluctuation measurements are not very fine, average fluctuation levels are used. The fluctuation levels are estimated for edge electron diamagnetic propagating components and edge ion diamagnetic propagating components separately. Since the propagation direction is opposite, the splitting of the two components is clear.

As shown in Fig. 20b, the fluctuation levels of the edge ion diamagnetic propagating components are clearly proportional to D_{edge} for all configurations, indicating that this component contributes to the edge diffusivity. However, edge electron diamagnetic components do not increase with an increase of D_{edge}. Further investigations are necessary to consider different roles of edge ion and electron diamagnetic components.

Figures 21a, 21b, and 21c show comparisons of density, temperature, and fluctuation amplitude profiles, respectively, for three different configurations ($R_{ax} = 3.6$, 3.75, and 3.9 m, $B_t = 1.49$, 1.5, and 1.54 T). The ion diamagnetic components are shown in Fig. 21c. The density profile is more or less similar for the three configurations. At more outward-shifted configurations, the ion diamagnetic fluctuation amplitude becomes larger, as shown in Fig. 21c, coincident with larger edge diffusion.

The spatial profiles of the gyro-kinetic linear growth rate of the ion temperature gradient mode (γ_{ITG}) calculated by the GOBLIN code[26] are shown in Fig. 21d. The growth rate does not vary much for the three different

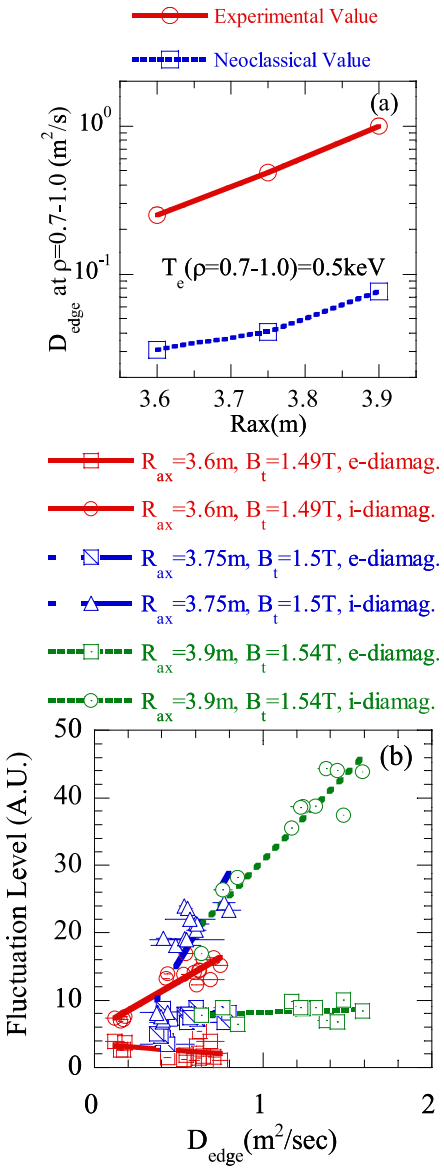

Fig. 20. (a) Dependences of D_{edge} on R_{ax}: $B_t = 1.49$ T for $R_{ax} = 3.6$ m, 1.5 T for $R_{ax} = 3.75$ m, and 1.54 T for $R_{ax} = 3.9$ m. Neoclassical values are calculated by GSRAKE. (b) Relation of D_{edge} and edge fluctuation level for three different configurations.[16]

configurations, although the ion diamagnetic fluctuation amplitude and D_{edge} show clearly different values. The growth rate is not the smallest for $R_{ax} = 3.6$ m, whose fluctuation amplitude and D_{edge} are the smallest. This indicates that the linear theory of ITG does not account for the observed turbulence fluctuations in the edge region of the data set analyzed here. However, the calculation of the γ_{ITG} does not take into account the effects of E_r, so the radial electric field shear may explain this because the linearly unstable turbulence fluctuations without E_r can be stabilized when the shearing rate exceeds

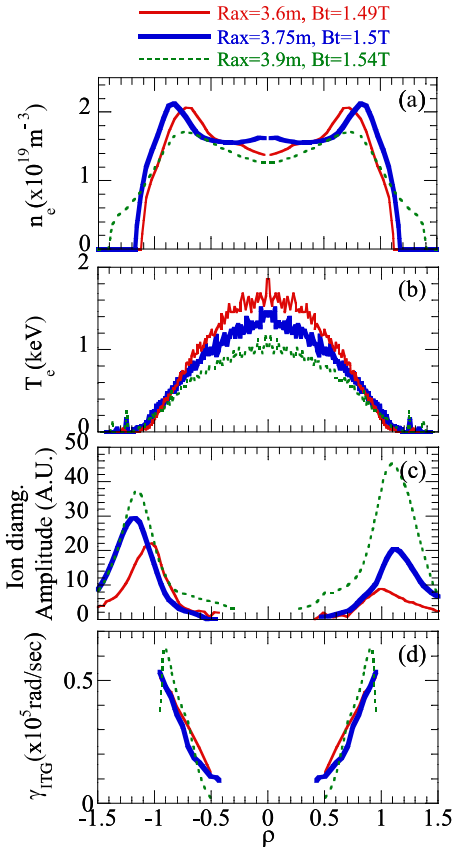

Fig. 21. (a) n_e, (b) T_e, (c) fluctuation amplitude profile of ion diamagnetic components, and (d) ITG growth rate $D_{edge} = 0.18$, 0.42, and 0.57 m^2/s at $R_{ax} = 3.6$, 3.75, and 3.9 m, respectively.[16]

growth rate.[27] For a detailed study, experimental measurements of E_r profiles are essential.

Also, additional studies in the core regions are necessary to understand the linkage between particle transport and turbulence in the core region. Because its transport and magnetic configuration characteristics are relatively simpler than those of the edge region, comparison with linear and nonlinear results is more straightforward. The upgraded PCI system can resolve core turbulence in space. Further analysis is now under way.

V.B. Turbulence Modeling

In the plasma core, where the particle source is negligible, the total flux becomes zero. Then, the diffusive flux and convective flux should be balanced as follows:

$$D\nabla n_e = n_e V \ . \tag{18}$$

Experimentally, this is shown at $\rho < 0.8$ in Fig. 18b. In the core region at $R_{ax} = 3.6$ m, the diffusive flux is dominated by anomalous driven flux and the convective flux for a hollow density profile is dominated by neoclassical flux as described in Sec. IV.B. In the positive gradient region of the hollow density profile (for example, at $\rho < 0.8$ of Fig. 18a), this indicates that the inward-directed anomalously dominated flux is balanced with the outward-directed neoclassically dominated flux. This qualitatively agrees with the prediction of quasi-linear theory. The particle flux calculated by the quasi-linear gyro-kinetic theory is directed inwardly in the positive gradient region of the hollow density profile.[26]

In a tokamak, neoclassical Ware pinch does not account for the observed inward pinch in the low-collisionality regime. The turbulence-driven thermodiffusive pinch and curvature pinch are candidates for the anomalous inward pinch.[28] The thermodiffusive pinch is proportional to the normalized T_e gradient and is directed inward (outward) with the increase (decrease) of R/L_{Ti} and with the decrease (increase) of T_e/T_i, where R is the major radius and L_{Ti} is ion temperature (T_i) scale length.[28] The curvature pinch is proportional to the normalized gradient of the safety factor (grad q/q).

For the large aspect ratio limit, the canonical density profile in a tokamak with circular cross sections is given as[21]

$$n_e(\rho) = n_e(0)\left[1 - \frac{4r_a}{3R_0}\int_0^{\rho} d\rho\left(\frac{d\ln q}{d\ln\rho} + \frac{3}{8}\right) + O\left(\frac{r_a^2}{R_0^2}\right)\right] , \tag{19}$$

where

r_a = minor radius

R_0 = major radius

ρ = normalized position

q = safety factor

O = integral term.

Equation (19) indicates that the density profile becomes peaked for positive magnetic shear (grad $q/q > 0$) and hollow for negative magnetic shear (grad $q/q < 0$). The former is a normal shear tokamak; the latter is a negative shear tokamak and LHD. This model assumes that the pinch term is only a curvature term and does not include other anomalous pinches such as the thermodiffusive pinch and the neoclassical pinch as well.

The curvature pinch was calculated for LHD taking into account the 3-D magnetic properties of LHD. Detailed formulations are described in Ref. 21. Figure 22 shows comparison of the experimental density profile and the modeled profile. A flat profile at $R_{ax} = 3.6$ m, $B_t = 2.75$ T and a hollow profile at $R_{ax} = 3.6$ m, $B_t = 1.49$ T are compared. In Fig. 22, the central density of the modeled profile was adjusted to the experimental value, since the canonical profile gives only a normalized profile. As shown in Fig. 22, the curvature profile predicts a

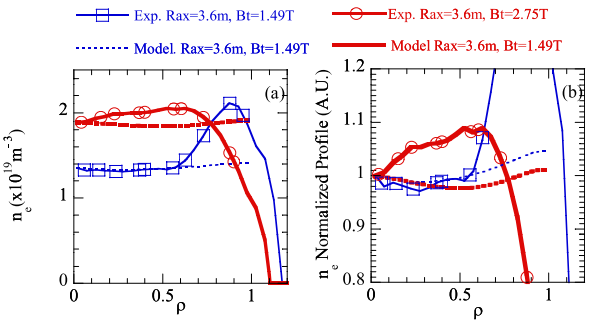

Fig. 22. Comparison of experimental density profile and curvature pinch model: (a) absolute profile and (b) expanded view of normalized profile.

very small positive gradient compared with the experimental profile in both cases. This indicates that the canonical curvature pinch model is not enough to account for the experimental profile. As described in Sec. IV.B, the neoclassical pinch is essential.

VI. DISCUSSION AND SUMMARY

Parameter dependences of particle transport coefficients of LHD were widely studied in the low-collisionality regime of the machine. It was found that particle transport was governed by R_{ax}, T_e, ν_h^*, B_t, and the injection direction of NBI; the latter distorted the flux surfaces and produced flat T_e and n_e profiles due to the formation of stochastic flux surfaces, so it is not due to the transport characteristics. To understand particle transport in LHD, analyses were carried out for experimental results of scans for the first four parameters.

Magnetic axis position is an easily controllable parameter and changes several magnetic properties. These were magnetic ripples, aspect ratios, safety factors, and plasma sizes. Among these parameters, magnetic ripples were the most widely variable, changing one order of magnitude. The magnetic ripples significantly affect neoclassical transport, meaning R_{ax} scans to be almost equivalent to studying the effects of neoclassical transport. Scans of T_e, ν_h^*, and B_t also change neoclassical properties of the plasma confinement and provide opportunities for studies over a wide range of experimental regions at each R_{ax}.

The obtained findings about the particle transport characteristics of LHD are described below.

In general, density profiles became more hollow with the increasing contribution of the neoclassical transport. Similar observations were reported in CHS (Ref. 29). Neoclassical transport in LHD increases at more outwardly shifted configurations and at lower collisionality. An exception to this general tendency was density profiles at $R_{ax} = 3.5$ m, where density profiles became more peaked at lower collisionality.

In Sec. IV, values of D and V were evaluated separately in the core ($\rho = 0.4$ to 0.7) and edge ($\rho = 0.7$ to 1.0) regions. In the following, we first discuss the core region, followed by a discussion of the edge region.

In general, core values of $D_{EXP.core}$ and $V_{EXP.core}$ determine the density profiles. In particular, the sign of $V_{EXP.core}$ determines whether the profile is peaked or hollow. Observed characteristics of $V_{EXP.core}$ may be classified into two groups. The first is the case when $V_{EXP.core}$ increases outward with an increase of T_e or a decrease of ν_h^*. These characteristics are observed at $R_{ax} = 3.6$, 3.75, and 3.9 m. Among these values of R_{ax}, 3.75 and 3.9 m yielded both experimentally evaluated and neoclassically calculated values of V_{core} that were directed outward, resulting in the density profiles always being hollow.

On the other hand, for $R_{ax} = 3.6$ m, $V_{EXP.core}$ changes direction from inward to outward with an increase of T_e or a decrease of ν_h^*, resulting in density profiles changing from peaked to hollow. In addition, it is to be noted that experimentally evaluated and neoclassically calculated values of V_{core} at $R_{ax} = 3.6$, 3.75, and 3.9 m have similar dependences on T_e and ν_h^* and their absolute values are about the same.

In this group, the neoclassical convection is mainly due to the thermodiffusion. Thus, density profiles are strongly affected by the neoclassical thermodiffusion. Similar observations are reported in W7-AS (Refs. 30 and 31) and the HSX (Ref. 32) stellarator. In W7-AS, the existence of an inward pinch in addition to neoclassical thermodiffusion was emphasized and the density profiles changed from flat to peaked, changing the normalized T_e gradient from a larger one to a smaller one.[30] This is in clear contrast to keeping almost a constant normalized T_e gradient while the density profile changed in LHD.

The second group is the case when $V_{EXP.core}$ increases inwardly with increasing T_e or decreasing ν_h^*, which was observed at $R_{ax} = 3.5$ m. A similar characteristic has been observed in most tokamak discharges.[5–7] In this case, dependences of $V_{EXP.core}$ on T_e and ν_h^* are opposite from those from the neoclassical prediction. This suggests the existence of an anomalous inwardly directed pinch. The turbulence-driven thermodiffusion may be one of the possible candidates, rather than the curvature pinch. In a tokamak, turbulence-driven thermodiffusion causes an inward pinch when ITG is the dominant instability.[28] It is not clear yet whether the ITG drives the inward pinch at $R_{ax} = 3.5$ m. Further investigation is necessary to understand this.

The larger values of $V_{EXP.core}$ at the more outwardly shifted magnetic axes (the larger values of R_{ax}) are attributable to the larger neoclassical contribution, which caused hollow density profiles as discussed above. However, the amount of neoclassical contribution is not the only quantity to determine whether the density profile is peaked or hollow. For example, the behavior of

$V_{EXP.core}$ for R_{ax} = 3.5 and 3.6 m was very different, as described in Secs. IV.A and IV.B, although values of $V_{NEO.core}$ for these two values of R_{ax} did not differ much, as shown in Figs. 12, 13, and 14. This suggests that the observed difference in the behavior of $V_{EXP.core}$ for R_{ax} = 3.5 and 3.6 m is not due to the difference in the neoclassical contribution but instead to that of the anomalous contribution. The turbulence might be more strongly destabilized at R_{ax} = 3.5 m. Parameters other than magnetic helical ripple may be more important for this case.

Next, we discuss core diffusion coefficients. Experimental values of D showed similar dependences on T_e and ν_h^* for all configurations; namely, values of D_{core} increased with increasing T_e or decreasing ν_h^*. Differences between experimentally evaluated and neoclassically calculated values of D_{core} become smaller at lower values of ν_h^*.

The core diffusion coefficients are also classified into two groups. At R_{ax} = 3.5 and 3.6 m, values of $D_{EXP.core}$ were more than one order of magnitude larger than those of $D_{NEO.core}$, whereas at R_{ax} = 3.75 and 3.9 m, those of $D_{EXP.core}$ were about twice those of the neoclassically calculated values.

At R_{ax} = 3.6 m, two comparisons of core particle transport with theoretical models were made. The gyrokinetic quasi-linear theory was shown to be in qualitative agreement with neoclassically calculated values of V_{core} and anomalously evaluated ones of D_{core} (Ref. 26). On the other hand, the curvature pinch model was unable to account for observed density profiles.[21]

Presently, values of $V_{EXP.edge}$ have not shown clear dependences on T_e and ν_h^*, suggesting an existence of some other ruling parameter. Values of $D_{EXP.edge}$ increased with increasing T_e or decreasing ν_h^*, with their absolute values being more than one order of magnitude larger than neoclassically calculated ones. Also, it is to be noted that edge diffusion processes were dominated by anomalous ones at all configurations, as evidenced in the observation that fluctuation levels increased with increasing $D_{EXP.edge}$.

It is difficult to say which R_{ax} shows the lowest particle transport. For example, at a representative value of T_e, R_{ax} = 3.75 m yields minimum values of both $D_{EXP.core}$ and $D_{EXP.edge}$, but the minimum exponent T_e was at R_{ax} = 3.6 m for both experimentally evaluated and neoclassically calculated values of D, suggesting that minimum D will be achieved at R_{ax} = 3.6 m for higher T_e.

Recent theoretical work shows that smaller ε_{eff}, where neoclassical transport is smaller, yields a larger residual zonal flow, which can suppress turbulence.[25,33] This statement is preferable because the reduction of neoclassical transport promises a reduction of anomalous transport. However, this is not the case for particle transport, as described in Sec. IV. At R_{ax} = 3.5 m, the $D_{EXP.core}$ and $D_{EXP.edge}$ were not the lowest, although the neoclassical values are lowest.

This paper treats the data set in the low-collisionality regime. A study of plasma behavior at high collisionality is important, because the recently achieved high-density operation of LHD using multiple pellet injections is believed to be one of the possible approaches to future reactor operation.[34,35] Some studies have already been carried out for this pellet-injected discharge,[2,36] and more detailed studies are now in progress.

The effects of the strength of magnetic fields, B_t, is not explained by the gyro-Bohm scaling. The results described in Sec. IV.C showed that the magnetic axis shifts due to higher β at lower field affect particle transport significantly. The dependence of $B_t^{1.5}$, which is expected from gyro-Bohm scaling, was not observed. However, more detailed investigations by changing the magnetic field widely are necessary. Also, the effects of the torque input due to NBI should be investigated in a future study.

In this paper particle transport was studied. However, the ultimate purpose of transport studies is to get clear knowledge to design a reactor. Other transports such as energy, helium, impurity, and momentum have to be investigated. The comparison between particle and energy transport will be done soon for the same discharge set analyzed in this paper.

ACKNOWLEDGMENTS

The authors are grateful to the LHD operation group for their excellent technical support. This work is supported by the budget NIFS05ULHH511 of the National Institute for Fusion Science.

REFERENCES

1. H. YAMADA et al., "Characterization of Energy Confinement in Net-Current Free Plasmas Using the Extended International Stellarator Database," *Nucl. Fusion*, **45**, 1684 (2005).

2. K. TANAKA et al., "Density Reconstruction Using a Multi-Channel Far-Infrared Laser Interferometer and Particle Transport Study of a Pellet-Injected Plasma on the LHD," *Plasma Fusion Res.*, **3**, 050 (2008).

3. K. NARIHARA et al., "Design and Performance of the Thomson Scattering Diagnostic on LHD," *Rev. Sci. Instrum.*, **72**, 1122 (2001).

4. K. TANAKA et al., "Experimental Study of Particle Transport and Density Fluctuations in LHD," *Nucl. Fusion*, **46**, 110 (2006).

5. H. TAKENAGA et al., "Comparisons of Density Profiles in JT-60U Tokamak and LHD Helical Plasmas with Low Collisionality," *Nucl. Fusion*, **48**, 075004 (2008).

6. C. BOURDELLE, "Turbulent Particle Trasnport in Magnetized Fusion Plasma," *Plasma Phys. Control. Fusion*, **47**, A317 (2005).

7. C. ANGIONI et al., *Proc. 36th Conf. Plasma Physics*, June 29–July 3, 2009, Sofia, Bulgaria, European Physical Society (2009).

8. M. SHOJI et al., "Three-Dimensional Proton Trajectory Analyses and Simulation of Neutral Particle Transport in an ICRF Heated Long Pulse Discharge on the Large Helical Device," *J. Nucl. Mater.*, **337–339**, 186 (2005).

9. K. TANAKA, "About the Correction of 'Experimental Study of Particle Transport and Density Fluctuations in LHD' on 2006 *Nucl. Fusion*, **46**, 110–122," *Nucl. Fusion*, **48**, 039801 (2008).

10. K. TANAKA et al., "Particle Transport and Fluctuation Characteristics Around the Neoclassically Optimized Configuration in LHD," *Plasma Fusion Res.*, **3**, S1069 (2008).

11. S. MURAKAMI et al., "Neoclassical Transport Optimization of LHD," *Nucl. Fusion*, **42**, L19 (2002).

12. C. D. BEIDLER and W. N. G. HITCHON, "Ripple Transport in Helical-Axis Advanced Stellarators: A Comparison with Classical Stellarator/Torsatrons," *Plasma Phys. Control. Fusion*, **36**, 317 (1994).

13. K. TANAKA et al., "Analysis Scheme for Density Modulation Experiments to Study Particle Confinements," *Plasma Sci. Technol.*, **8**, 65 (2006).

14. D. REITER, P. BOGEN, and U. SAMM, "Measurements and Monte Carlo Computations of Hα Profiles of a TEXTOR Limiter," *J. Nucl. Mater.*, **198–198**, 1059 (1992).

15. N. J. LOPES CARDOZO, "Perturbative Transport Studies in Fusion Plasmas," *Plasma Phys. Control. Fusion*, **37**, 799 (1995).

16. K. TANAKA et al., "Effect of Magnetic Configuration on Particle Transport and Density Fluctuation in LHD," *Fusion Sci. Technol.*, **51**, 97 (2007).

17. V. TRIBALDOS, "Monte Carlo Estimation of Neoclassical Transport for the TJ-II Stellarator," *Phys. Plasmas*, **8**, 1229 (2001).

18. K. IDA et al., "Observation of an Impurity Hole in a Plasma with an Ion Internal Transport Barrier in the Large Helical Device," *Phys. Plasmas*, **16**, 056111 (2009).

19. K. IDA et al., "Bifurcation Phenomena of a Magnetic Island at a Rational Surface in a Magnetic-Shear Control Experiment," *Phys. Rev. Lett.*, **100**, 045003 (2008).

20. M. YAKOVLEV et al., "Heat Pulse Propagation Across the Rational Surface in a Large Helical Device Plasma with Counter-Neutral Beam Injection," *Phys. Plasmas*, **12**, 1 (2005).

21. A. MISHCHENKO, P. HELANDER, and Y. TURKIN, "Curvature Particle Pinch in Tokamak and Stellarator Geometry," *Phys. Plasmas*, **14**, 102308 (2007).

22. A. L. SANIN et al., "Two Dimensional Phase Contrast Interferometer for Turbulence Study on LHD," *Rev. Sci. Instrum.*, **75**, 3439 (2004).

23. C. A. MICHAEL et al., "Upgraded Two-Dimensional Phase Contrast Imaging System for Fluctuation Profile Measurement on LHD," *Rev. Sci. Instrum.*, **77**, 10E923 (2006).

24. K. TANAKA et al., "Two Dimensional Phase Contrast Imaging for Local Turbulence Measurements in LHD," *Rev. Sci. Instrum.*, **79**, 10E702 (2008)

25. T.-H. WATANABE, H. SUGAMA, and S. FERRANDO-MARGALET, "Gyrokinetic Simulation of Zonal Flows and Ion Temperature Gradient Turbulence in Helical Systems," *Nucl. Fusion*, **47**, 1383 (2007).

26. O. YAMAGISHI et al., "On the Particle Fluxes and Density Profiles in Helical Systems," *Phys. Plasmas*, **14**, 012505 (2007).

27. T. S. HAHM and K. H. BURRELL, "Flow Shear Induced Fluctuation Suppression in Finite Aspect Ratio Shaped Tokamak Plasma," *Phys. Plasmas*, **2**, 1648 (1995).

28. C. ANGIONI et al., "Density Response to Central Electron Heating: Theoretical Investigations and Experimental Observations in ASDEX Upgrade," *Nucl. Fusion*, **44**, 827 (2004).

29. H. IGUCHI et al., "The Effect of Magnetic Field Configuration on Particle Pinch Velocity in Compact Helical System," *Plasma Phys. Control. Fusion*, **36**, 1091 (1994).

30. U. STROTH et al., "Evidence for Convective Inward Particle Transport in a Stellarator," *Phys. Rev. Lett.*, **82**, 928 (1999).

31. J. P. T. KOPONEN et al., "Perturbative Particle Transport Studies in the W7-AS Stellarator," *Nucl. Fusion*, **40**, 365 (2000).

32. J. M. CANIK, "Experimental Demonstration of Improved Neoclassical Transport with Quasihelical Symmetry," *Phys. Rev. Lett.*, **98**, 085002 (2007).

33. H. SUGAMA and T. H. WATANBE, "Dynamics of Zonal Flows in Helical Systems," *Phys. Rev. Lett*., **94**, 115001 (2005).

34. H. YAMADA et al., "Characterization and Operational Regime of High Density Plasmas with Internal Diffusion Barrier Observed in the Large Helical Device," *Plasma Phys. Control. Fusion*, **49**, B487 (2007).

35. R. SAKAMOTO et al., "Pellet Injection and Internal Diffusion Barrier Formation in Large Helical Device," *Plasma Fusion Res.*, **2**, 047 (2007).

36. K. TANAKA et al., "Temporal Evolution of Particle Transport of Super Dense Core Plasma in LHD," *J. Phys.: Conf. Ser.*, **123**, 012020 (2008).